Geophysical Journal International

Anatomy of strong ground motion: near-source records and three-dimensional physics-based numerical simulations of the M_W 6.0 2012 May 29 Po Plain earthquake, Italy

R. Paolucci,[1] I. Mazzieri[2] and C. Smerzini[1]

[1]*DICA-Department of Civil and Environmental Engineering, Politecnico di Milano, Piazza Leonardo da Vinci 32, I-20133 Milano, Italy*
[2]*MOX-Laboratory for Modeling and Scientific Computing, Department of Mathematics, Politecnico di Milano, Piazza Leonardo da Vinci 32, I-20133 Milano, Italy. E-mail:* ilario.mazzieri@polimi.it

SUMMARY

Stimulated by the recent advances in computational tools for the simulation of seismic wave propagation problems in realistic geological configurations, this paper presents a 3D physics-based numerical analysis of near-source ground motion during the M_W 6.0 2012 May 29 earthquake in the Po Plain, Northern Italy. To reproduce with sufficient accuracy some of the most peculiar features of the near-source strong-motion records and of the spatial variability of damage distribution, this study required a sequence of investigations, starting from the analysis of a wide set of near-source records, to the calibration of an improved kinematic seismic source model, up to the development of a 3D numerical model of the portion of the Po Plain interested by the earthquake. The latter includes the basin geometry, characterized by sediment thickness sharply varying from few tens of metres to some kilometres. The spatial resolution of the numerical model is suitable to propagate frequencies up to about 1.5 Hz. Numerical simulations were performed using the open-source high-performance code SPEED, based on the Discontinuous Galerkin Spectral Elements method. The 3D numerical model, coupled with the updated slip distribution along the rupturing fault, proved successful to reproduce with good agreement, measured through quantitative goodness-of-fit criteria, the most relevant features of the observed ground motion. These include: (i) the large fault normal velocity peaks at the near-source stations driven by updip directivity effects; (ii) the small-scale variability at short distance from the source, resulting in the out-of-phase motion at stations separated by only 3 km distance; (iii) the propagation of prominent trains of surface waves, especially in the Northern direction; (iv) the map of earthquake-induced ground uplift with maximum values of about 10 cm, in substantial agreement with geodetic measurements and (v) the two-lobed pattern of the peak ground velocity map, well correlated with the distribution of macroseismic intensity.

Key words: Earthquake ground motions; Site effects; Computational seismology; Wave propagation.

1 INTRODUCTION

Between 2012 May and June, a sequence of earthquakes struck a densely populated area in the Po Plain, about 20 km north of Modena and west of Ferrara, in the Emilia-Romagna region, Northern Italy, causing 27 fatalities and substantial damage especially to industrial facilities and historical monuments. The sequence started with a M_W 6.1 event (source: Regional Centroid Moment Tensor (RCMT), http://www.bo.ingv.it/RCMT) on May 20, at 02:03:53 (UTC), with epicentre near the town of Finale Emilia. In the following days, the seismic sequence migrated Westwards and culminated, on May 29,

at 07:00:03 (UTC), with a second relevant shock of M_W 6.0 (source: RCMT, http://www.bo.ingv.it/RCMT), about 10 km SW of the May 20 event, with epicentre close to the municipalities of Mirandola and Medolla. On June 3, an M_L 5.1 event, in the municipality of Novi di Modena, closed the Po Plain seismic sequence. The superimposition of the effects of these events made the macroseismic survey difficult, since the assessment of Mercalli–Cancani–Sieberg (MCS) intensity values was influenced by the cumulative effects of the entire seismic sequence (Galli *et al.* 2012). For this reason the largest intensity $I_{MCS} = 7$–8 was estimated in the municipality of Novi di Modena where the last shock occurred. In spite of the relatively modest
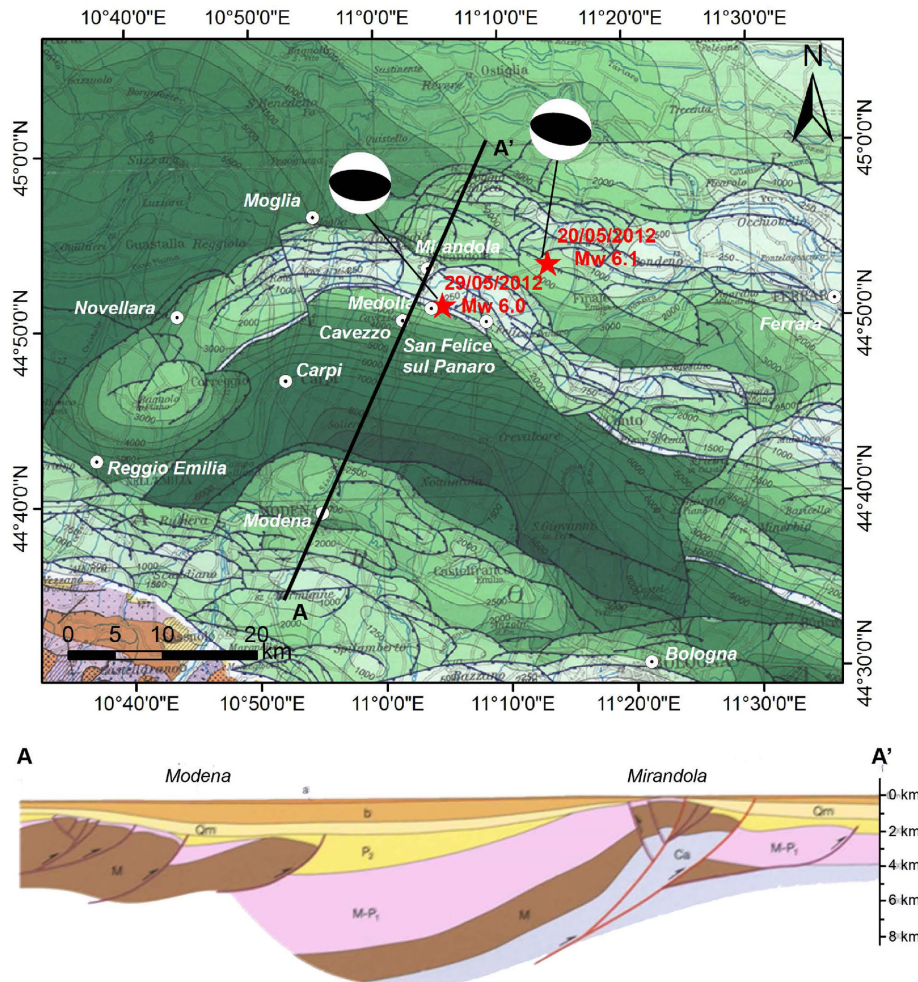
Figure 1. Top panel: structural map of Italy, reproduced from Bigi *et al.* (1992), where the different shades of green denote the depth of the base of Pliocene; the epicentres (stars) and focal mechanisms of the two main shocks of the Po Plain seismic sequence on 2012 May 20 (M_W 6.1) and May 29 (M_W 6.0) are also indicated. Focal mechanisms are from the time domain moment tensors (TDMT) database, http://cnt.rm.ingv.it/tdmt. Bottom panel: simplified geological cross-section **A–A′** passing through the Ferrara-Romagna folded arc and showing the structural high close to the town of Mirandola (from Boccaletti *et al.* 2010). (a) Middle (0.45 My–Present); (b) Middle Pleistocene (1–0.45 My); Qm: Early Pleistocene (1.8–1 My); P_2: Middle-Late Pliocene (4.1–1.8 My); M-P_1: Late Messinian–Early Pliocene (6.3–4.1 My); M: Miocene (24–5.4 My); Ca: Meso-Cenozoic carbonatic succession (227–24 My).

effects on residential buildings, the earthquakes caused devastating damage to historical and industrial structures, with a dramatic economic impact estimated to about 13 billion Euros of overall loss (Munich RE 2015).

The seismic sequence occurred in the Southern portion of the Po Plain, a subsident EW trending foreland basin of two opposite verging fold-and-thrust belts, the Southern Alps to the north and the Northern Apennines to the south, which developed in response to the collision of the African and European plates from the Cretaceous onward (Burrato *et al.* 2012). The Po Plain is filled by Plio-Quaternary marine and continental deposits, whose thickness ranges from a few tens of metres at the top of buried anticlines up to about 8 km in the Eastern part of the basin toward the Adriatic sea (Bigi *et al.* 1992).

Data on the shallow and deep geological setting of the Po Plain have been mostly gathered in the framework of extensive hydrocarbon exploration, conducted in the 1970s and 1980s (Pieri & Groppi 1981; Cassano *et al.* 1986; Bigi *et al.* 1992; Fantoni & Franciosi 2010), hydrological studies (RER 1998) and the new geological map of Italy (1:50,000 scale, http://sgi.isprambiente.it). The contour lines describing the base of the Pliocene-Quaternary

sequence are available in the Structural Model of Italy (Bigi *et al.* 1992) and are reproduced in Fig. 1. More recently, the depths of the main geological interfaces were reassessed by Molinari *et al.* (2015), who proposed a 3D seismic model of the Po Plain over an area of about 600 km by 300 km, based on an extensive set of geological and geophysical data, including seismic reflection and refraction profiles, borehole logs and geological maps.

The Northern Apennines frontal thrust system is composed of a pile of NE-verging tectonic units that have developed as a consequence of the Cenozoic collision between the European plate and the Adria plate (Boccaletti *et al.* 2004). The outermost sector of this system, corresponding to the Po Plain, consists of a complex system of thrust faults and folded arcs, namely, Monferrato, Emilia and Ferrara-Romagna, from west to east, which locally generated structural highs (Fig. 1). The 2012 Emilia seismic sequence reactivated the basal thrust in the central section of the Ferrara-Romagna arc, as illustrated in Fig. 1, around the town of Mirandola. The spatial distribution of the aftershocks together with the available focal solutions indicate that the activated fault system covers a relatively large area elongated in the EW direction (about 50 km

long) and consists of nearly EW-striking thrust fault sources dipping south.

The seismic sequence was recorded by different accelerometer networks operating on the Italian territory, making available a wide high-quality data set of recordings in the near field of a thrust event within a region of moderate seismicity and characterized by a very deep sedimentary structure such as the Po Plain. This study is entirely devoted to the analysis of the May 29 earthquake, which is the best documented in terms of strong-motion (SM) records, because many temporary stations were installed in the aftermath of the main shock of May 20.

From the discussion above, it is clear that the May 29 earthquake presents several unique features, that make its study challenging from the point of view of earthquake ground motion characterization, namely: (i) the complex geological setting of a deep and large sedimentary basin such as the Po Plain, with sharp variability of sediment thickness, from a few tens of metres to about 8 km; (ii) the availability of a nearly unique near-fault SM data set on deep and soft sediments in the context of a region of moderate seismicity.

Stimulated by these considerations, this paper aims at studying within a broad perspective the 2012 May 29 Po Plain earthquake, ranging from the analysis of the near-source SM data set, to the improvement of the available kinematic source models, up to the 3D physics-based numerical simulation of seismic ground shaking. These were performed using SPEED—Spectral Elements in Elastodynamics with Discontinuous Galerkin (http://speed.mox.polimi.it), an innovative high-performance computer code, suitable to tackle multiscale seismic wave propagation problems in heterogeneous media.

The first section of the paper illustrates the May 29 earthquake SM data set, focusing on the near-source records and on the spatial distribution of peak ground motion values, in comparison with that provided by ground motion prediction equations (GMPEs). Then, an updated slip distribution model is introduced, calibrated on the near-source records, which provides evidence of updip directivity effects on earthquake ground motion. Finally, 3D physics-based numerical simulations of the 2012 May 29 earthquake are presented, spanning a frequency range up to about 1.5 Hz. A thorough check of numerical results versus observations is introduced, including comparison in time and frequency domain, as well as quantitative goodness-of-fit (GoF) tests. Ground motion maps are also presented, in terms of permanent ground uplift and of peak ground velocity, and compared with both instrumental and macroseismic observations.

2 NEAR-SOURCE STRONG-MOTION RECORDS

In this section, some features of the near-source strong-motion data set generated by the May 29 earthquake are addressed. Referring to Luzi *et al.* (2013) and Castro *et al.* (2013) for an overview of the SM records of the entire 2012 Po Plain seismic sequence, we have limited our attention to 34 stations which recorded the earthquake within an epicentral distance $R_e < 30$ km (Table 1). These stations mostly belong to the Italian SM network (RAN) and to temporary networks operated by the Italian Department of Civil Protection (DPC) and by the National Institute of Geophysics and Volcanology (INGV), installed after the May 20 main shock. Corrected records were downloaded from the Italian Accelerometric Archive ITACA (http:// itaca.mi.ingv.it/).

Stations are classified based on the average shear wave velocity of the uppermost 30 m, $V_{S,30}$, according to Eurocode 8, EC8

(CEN 2004). Symbol $*$ in the soil classification means that soil class is inferred from geological considerations, rather than being based on direct measurements of the shear wave velocity. Due to the relatively homogeneous shallow soil conditions throughout the epicentral area, all sites were assumed to belong to soil class C ($V_{S,30}$ in the range 180–360 m s^{-1}). As a matter of fact, in such area $V_{S,30}$ is typically found to range from 200 to 250 m s^{-1}.

For each SM station in Table 1, peak ground acceleration (*PGA*), peak ground velocity (*PGV*) and peak ground displacement (*PGD*) values are provided in terms of the fault normal (FN) and vertical (UP) components, as well as the FN/FP (fault parallel) ratio. Note that, since the fault strike is predominantly EW (95°), the FN component is very close to NS. In Fig. 2, the variation with R_e of both FN and FP components of *PGA* and *PGV* is shown together with the GMPE of Bindi *et al.* (2014), referred to as BI14 hereafter, in terms of geometric mean of horizontal components. The BI14 relationship was derived from Italian data, including the Po Plain seismic sequence. Note that, for this comparison, the BI14 coefficients for the hypocentral distance, R_{hypo}, were used, considering the focal depth of the May 29 earthquake, equal to 10.2 km. In Fig. 3 a representative selection of velocity time histories (NS component) is presented to illustrate the large variability of amplitude and characteristics of seismic shaking with distance and azimuth. This is also highlighted by the selection in Fig. 4, which shows the NS velocity (left) and displacement (right) waveforms recorded by an array of temporary stations (referred to as MIR hereinafter), installed by the INGV rapid response network for site effects EMERSITO, after the May 20 main shock (Bordoni *et al.* 2012). The MIR array consists of eight stations aligned along a roughly S-N trending profile, following the direction of increasing thickness of the sediment cover, toward the Po river, from the Mirandola buried structural high (see Fig. 1).

These SM accelerograms form a wide set of near-source records for reverse-fault earthquakes on deep soil configurations, that will be the basis for the validation of the numerical simulations illustrated in the next sections of this study. For sake of brevity, we limit ourselves here to summarize some of their most relevant features:

(1) Prevailing FN motion is apparent in the range $R_e \leq 10$ km, with average FN/FP values ranging from 1.2 for *PGA*, to 1.8 for *PGV* and 2.0 for *PGD*, as expected because in the near-source region the displacement tends to be oriented as the fault slip vector.

(2) For $R_e > 10$ km, FN/FP is significantly larger than 1 (FN/FP$_{avg}$ = 1.5) only for *PGD*, probably owing to the dominance of long-period surface waves propagating Northwards, as a consequence of the configuration of the buried topography of the area (see Fig. 1).

(3) FN *PGV* values tend to lie between the 50th and 84th percentile of BI14 at distances less than 15 km approximately.

(4) Velocity pulses with prevailing period of around 1.5 s in the FN direction are evident up to about 5 km distance from the epicentre, while, for increasing distances, trains of surface waves become dominant, as can be clearly seen within the MIR array records (Fig. 4).

(5) Very large values of vertical *PGA* are observed, with an impressive 840 cm s^{-2} at MRN, in agreement with the frequent finding, in near-source records, of prevailing vertical *PGA* with respect to the horizontal one (see e.g. Ambraseys & Douglas 2003).

(6) A large small-scale spatial variability is noted, especially when comparing SM records MIR01 and MIR02 in Fig. 4, at some 3 km distance: although records look similar at a first glance, there is a clear out-of-phase motion that suggests a major influence of the

Table 1. Overview of the SM data set recorded during the 2012 May 29 Po Plain earthquake at epicentral distance $R_e < 30\,\mathrm{km}$. Fault normal (FN), fault parallel (FP) and vertical (UP) *PGA*, *PGV* and *PGD* values are provided.

| Station code	Lat (°N)	Lon (°E)	Soil class	R_e (km)	PGA_{FN} (cm s^{-2})	$\frac{PGA_{FN}}{PGA_{FP}}$	PGA_{UP} (cm s^{-2})	PGV_{FN} (cm s^{-1})	$\frac{PGV_{FN}}{PGV_{FP}}$	PGV_{UP} (cm s^{-1})	PGD_{FN} (cm)	$\frac{PGD_{FN}}{PGD_{FP}}$	PGD_{UP} (cm)
MIR01	44.844	11.071	C*	1.41	382.1	0.96	361.5	53.0	1.75	13.8	21.1	2.52	5.1
MRN	44.878	11.062	C	4.10	289.2	1.32	840.6	58.1	2.14	26.8	14.7	1.80	5.8
MIR02	44.887	11.073	C*	4.12	238.8	1.08	452.3	55.2	1.66	12.0	16.3	1.53	5.0
SAN0	44.838	11.143	C*	4.70	217.0	1.22	307.8	33.6	1.55	8.7	10.3	1.22	3.0
MIR08	44.917	11.090	C*	7.33	246.7	1.14	306.7	32.3	1.89	7.8	10.2	3.78	4.2
T0802	44.875	11.182	C*	8.01	286.6	1.10	176.5	25.0	1.46	5.2	7.9	1.29	1.9
T0813	44.878	11.199	C*	9.43	339.6	0.95	171.1	24.8	1.15	3.8	6.2	1.10	2.1
MIR03	44.938	11.105	C*	9.82	328.3	1.52	398.3	34.0	2.52	6.9	7.8	2.28	2.6
T0818	44.935	11.030	C*	10.30	274.3	1.10	210.6	39.1	2.00	6.7	9.0	3.15	3.1
MIR04	44.927	11.178	C*	11.20	324.0	0.85	258.3	28.2	0.81	5.7	6.2	0.83	2.2
T0814	44.793	10.969	C*	11.24	506.1	1.16	252.5	21.6	0.89	6.1	6.3	1.44	1.7
T0800	44.849	11.248	C*	12.80	246.4	0.75	331.8	20.0	0.72	5.0	3.2	0.65	0.8
T0811	44.784	11.227	C*	13.39	195.1	1.00	124.3	24.3	1.49	2.8	4.1	1.38	0.6
T0812	44.955	11.181	C*	13.75	185.6	1.41	108.8	17.8	1.64	2.9	7.1	1.87	1.4
MIR05	44.981	11.107	C*	14.52	264.6	1.64	148.9	20.7	1.41	4.3	7.4	2.30	1.7
SMS0	44.934	11.235	C*	15.00	176.7	1.06	104.3	14.0	1.00	3.0	4.4	1.07	1.1
RAV0	44.716	11.143	C*	15.70	79.0	1.27	61.8	9.7	1.41	1.6	4.3	2.85	1.2
FIN0	44.830	11.287	C*	16.00	226.8	1.09	189.1	16.5	0.91	3.0	2.8	0.90	0.9
T0824	44.759	10.928	C*	16.15	159.2	0.73	96.4	15.6	1.19	2.6	3.0	1.11	0.8
MOG0	44.932	10.912	C*	16.40	176.7	0.77	124.2	21.6	0.79	5.0	6.4	1.92	1.6
CRP	44.782	10.870	C*	18.70	172.9	1.47	83.2	6.6	0.73	2.2	1.9	0.89	0.7
T0805	44.919	11.323	C*	20.15	150.8	0.62	69.2	8.1	0.63	1.5	2.3	0.68	0.7
MIR06	45.040	11.087	C*	21.02	115.7	1.20	89.4	17.8	2.91	2.6	6.3	5.51	1.0
CNT	44.723	11.287	C*	21.30	290.8	1.35	63.8	13.5	0.77	2.6	2.7	0.75	0.7
T0803	44.767	11.351	C*	22.94	70.1	0.58	66.6	8.0	0.92	2.0	2.4	1.49	0.3
SERM	45.010	11.296	C*	24.22	14.9	1.03	9.0	1.8	1.71	0.3	1.0	2.14	0.2
SAG0	44.791	11.390	C*	25.00	64.9	0.81	65.5	5.9	0.76	2.2	1.6	1.02	0.6
MIR07	45.081	11.130	C*	25.80	62.4	0.82	60.9	12.0	1.71	2.7	5.4	2.39	0.7
CAS05	44.802	11.410	C*	26.17	57.4	0.68	46.2	4.3	0.63	1.6	1.4	0.78	0.8
CAS0	45.025	11.311	C*	26.30	41.2	0.60	29.7	6.7	0.88	1.3	3.7	1.75	0.5
BON0	44.886	11.418	C*	26.50	24.8	0.71	30.2	2.8	1.28	1.2	1.5	1.47	0.3
MODE	44.630	10.949	C*	26.87	19.3	0.42	42.3	3.0	0.72	2.2	1.6	0.72	0.8
MDN	44.647	10.890	C	27.50	51.7	1.72	35.1	3.7	1.36	2.0	1.5	1.28	0.6
NVL	44.842	10.731	C	28.10	47.5	0.88	46.2	2.8	1.11	1.1	0.9	1.23	0.3
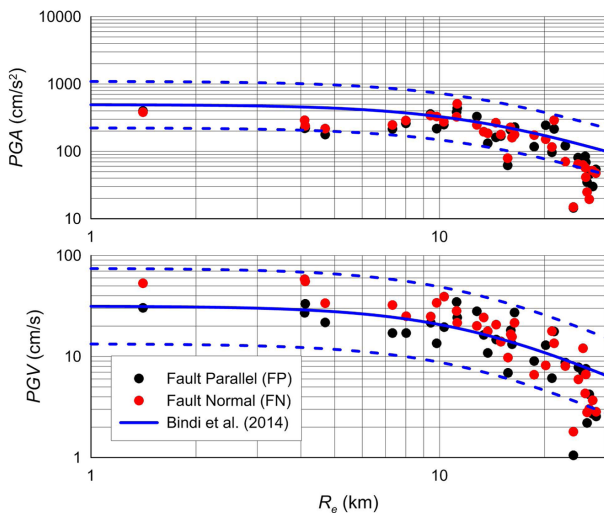
Figure 2. Fault normal (FN) and fault parallel (FP) components of *PGA* (top) and *PGV* (bottom) in the selected SM data set of the 2012 May 29 earthquake. Data from ITACA database. The GMPE of Bindi *et al.* (2014), geometric mean of horizontal components, is also shown.

focal mechanism itself, with a nodal line probably passing about half way between the two stations.

To investigate in more detail the spatial distribution of earthquake ground motion, with possible combined effect of the seismic source and of the irregular subsoil configuration, residuals between recorded peak ground motions and the ones predicted by the GMPE of BI14 are analysed. To this end, we computed for each station the ratio of the recorded peak ground motion, that is, *PGA*, *PGV* and $S_a(2s)$, the latter being the pseudo-acceleration response spectral (RS) ordinate at $T = 2\,\mathrm{s}$, with respect to the corresponding value from the BI14. $S_a(2s)$ was selected because it is representative of the range of long vibration periods of flexible structures, such as precast industrial buildings and monumental towers, which suffered the most relevant damage during the earthquake. Predictions are computed for reverse focal mechanisms and for sites C in the EC8 soil classification, considering $M_W = 6$. The Joyner–Boore (R_{JB}) distance, used herein in BI14, was computed by considering the fault geometry adopted in the numerical model and shown in Fig. 3. Note that, although BI14 holds for the geometric mean of the two horizontal components, we decided to compare it with the recorded peak FN values, the geometric mean being hardly meaningful for directional motions in near-source conditions. Fig. 5 shows such a comparison, whence it can be deduced that:
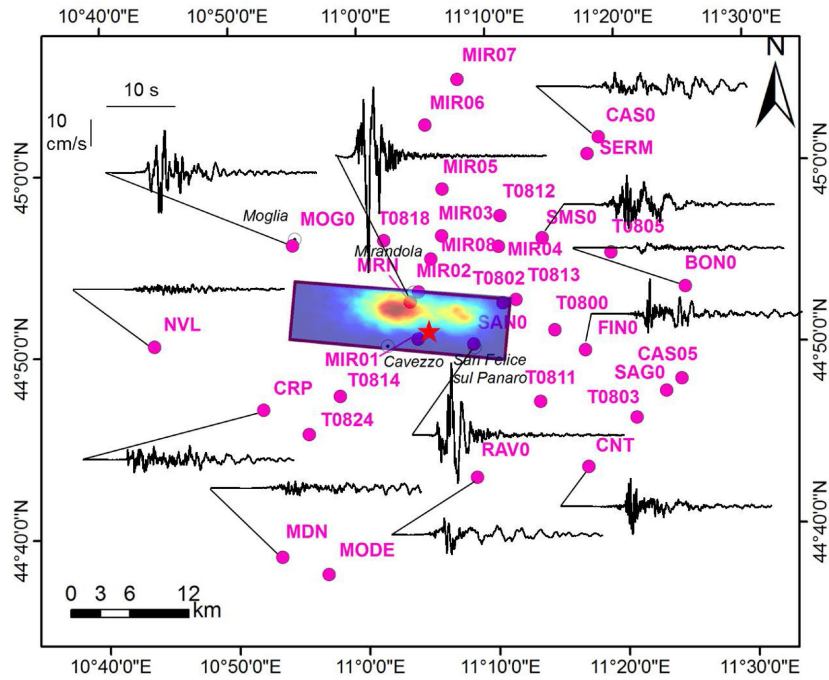
Figure 3. Spatial variability of the NS velocity records in the epicentral area of the May 29 earthquake at selected SM stations. The kinematic fault model, as implemented in the 3D numerical simulations, is also superimposed.
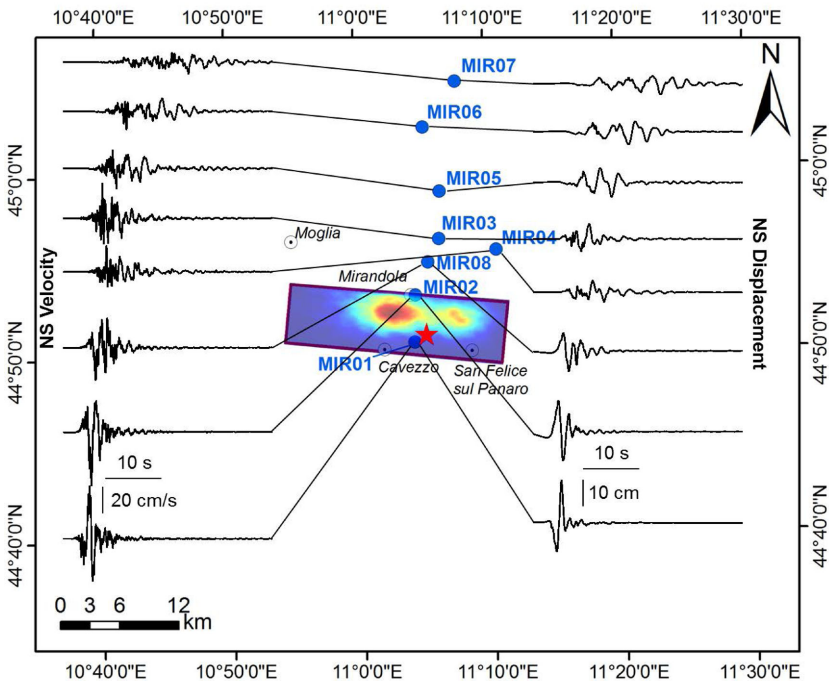
Figure 4. NS records along the MIR transect in terms of both velocity (left-hand side) and displacement (right-hand side) waveforms. The kinematic fault model, as implemented in the 3D numerical simulations, is also superimposed.

(1) Records of the May 29 earthquake have generally lower horizontal *PGA*s than predicted by BI14, implying possible non-linear effects at high frequencies.

(2) *PGV*s are underestimated by a factor up to about 2, moving Northwards from the seismic source.

(3) A similar trend as for *PGV*, although substantially amplified, can be observed also for $S_a(2s)$, for which the underestimation in the stations located north of the

seismic source is even larger, reaching up to a factor of 4.

The latter underestimations, either in terms of *PGV* or $S_a(2s)$, may be mostly attributed to a combination of: (1) the inadequacy of the geometric mean to predict highly directional ground motions in the near-source region and (2) the inadequacy of $V_{S,30}$ as a proxy for very deep soil sediments, the seismic response of which may
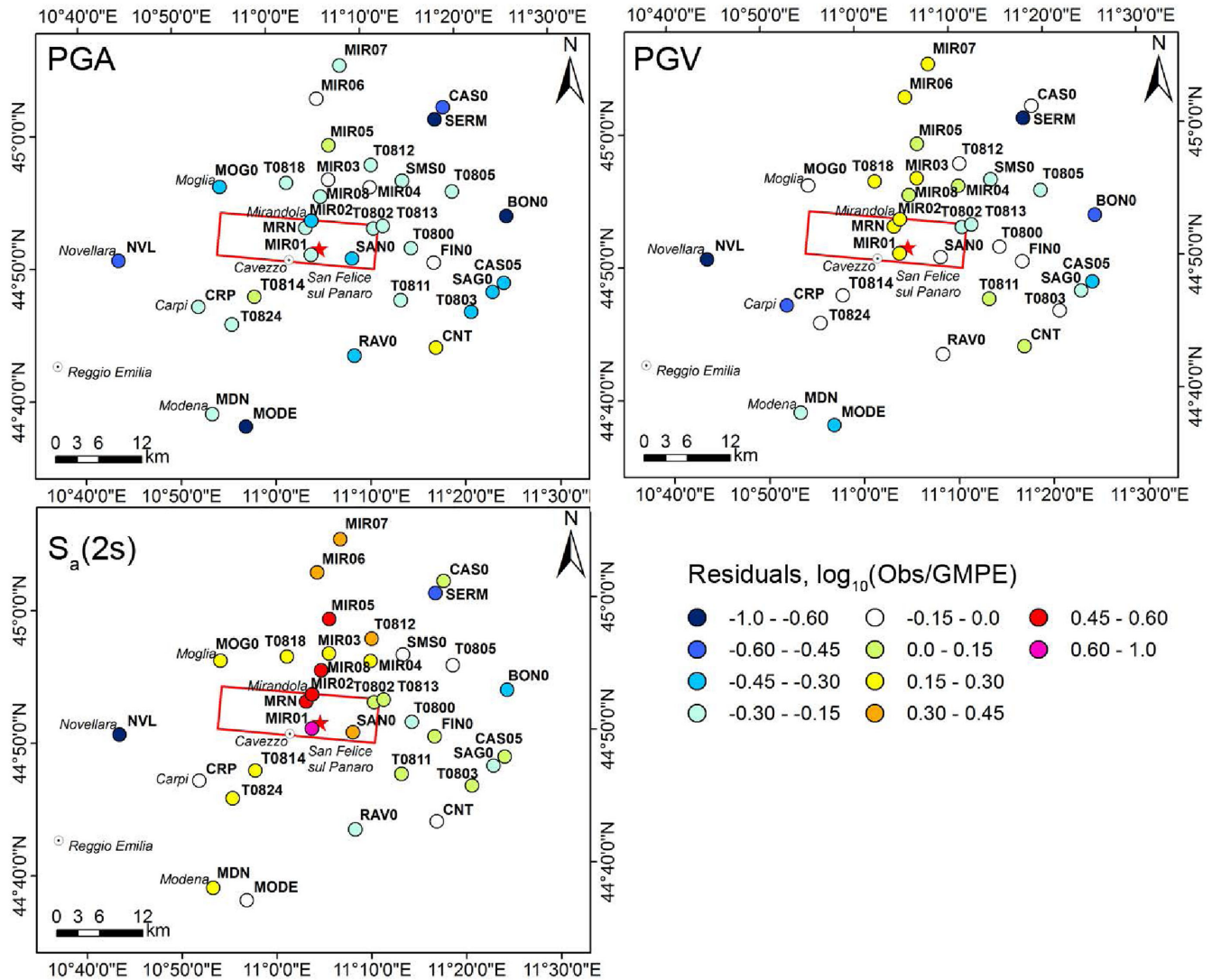
Figure 5. Residuals, computed as log$_{10}$(observed/predicted), with respect to the GMPE of Bindi *et al.* (2014). Comparison is made in terms of the observed FN components of *PGA* (top panel, left), *PGV* (top panel, right) and $S_a(2s)$ (bottom, left).
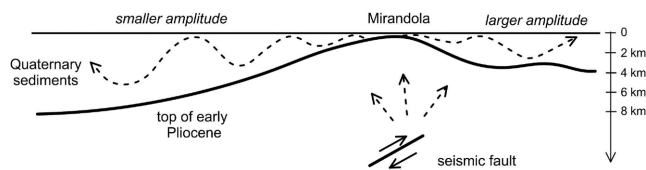

Figure 6. Sketch for interpretation of the observed features of ground motion in terms of coupling of seismic source effects and complex submerged geology.

be better approximated by assuming softer soil conditions (Class D, $V_{S,30} < 180\,\mathrm{m\,s^{-1}}$) than used in the GMPE.

A sketch summarizing some of the main factors affecting near-source ground motion during the Po Plain earthquake of May 29 is illustrated in Fig. 6, with emphasis on the interaction of buried topography with generation of prominent surface waves produced by the highly irregular geological configuration underneath the epicen-

tral region. This sketch clearly points out the need of 3D numerical modeling, to properly simulate the coupling of the kinematics of the seismic source with the complex geological conditions.

We finally note that one of the clearest features of observed ground motion discussed in this section, that is, the prevailing FN (roughly NS) component of motion, had a major role on the onset of damage, particularly for those structures responding in the period range from 1 to 2 s where the largest energy content of ground motion was concentrated, as shown by the near-source velocity pulses. This is the case of many churches and industrial pre-cast structures, which actually suffered the highest level of damage during these earthquakes. Fig. 7, showing the partial collapse of the San Francesco Church, in Mirandola, only 500 m away from the MIR02 station, provides an impressive example of such damage. As a matter of fact, the nave, with longitudinal axis roughly oriented EW, as in most of the ancient Catholic churches, collapsed in the NS direction, while the facade, much stiffer in its plane, remained nearly intact.

Figure 7. Collapse of the San Francesco Church (XV century), Mirandola. Courtesy of A. Penna.

Table 2. 1D seismic model adopted for the simulations with the Hisada approach. z_b denotes the depth of the base of the layer, ρ the soil density, V_S and V_P the S- and P-wave velocities and Q_S the S-wave quality factor.

z_b (m)	ρ (kg m^{-3})	V_S (m s^{-1})	V_P (m s^{-1})	Q_S ($-$)
150	1800	250	1500	25
500	2100	800	1800	80
1000	2100	1200	2300	150
3000	2200	2100	3500	200
6000	2400	2750	4750	250
>6000	2800	3670	6340	350

3 ADJUSTMENT OF THE FAULT-SLIP PARAMETERS BASED ON NEAR-SOURCE GROUND MOTION RECORDS

The adjustment of the slip distribution source model of the May 29 earthquake was by far the most demanding task to obtain an overall satisfactory agreement of the numerical simulations with the near-source records introduced in the previous section.

We started from a slip model inverted soon after the earthquake based on observed coseismic deformations (Atzori, personal communication, 2012) and checked its accuracy against near-source SM records. This was done by considering this model as the input for earthquake ground motion simulations by the Hisada approach (Hisada & Bielak 2003), assuming a horizontally layered crustal model as shown in Table 2. This model approaches, within the area of Mirandola, the 1D seismic profile estimated by Milana *et al.* (2014), based on the inversion of SM records and microtremors. For this reason, the 1D approximation applies only at few stations, tentatively MIR01, MIR02, MRN and SAN0 (see Fig. 3 for location), while, as the thickness of the Quaternary sediments increases, either moving N or S (see Fig. 1), a 1D model is no longer suitable to capture the most important features of ground motion, both in terms of frequency and arrival times, as it will be discussed later.

Subsequently, a trial-and-error procedure was followed to improve the agreement with records by changing the parameters of the main asperities (slip amplitude, depth, along strike position), while keeping the position of the hypocentre unchanged, after
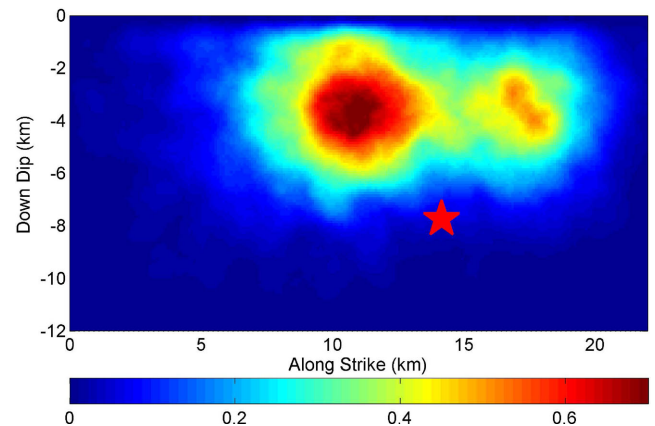

Figure 8. Slip distribution proposed in this work to optimize the agreement with near-source SM records. Scale of slip in metres. Note that the vertical axis denotes the downdip direction and its origin lies at 3.7 km depth (see Table 3).

verification of consistency of waveform arrivals with the assumed crustal model (Herrero, personal communication, 2014), and checking the fit between synthetics and recordings. The resulting slip distribution is shown in Fig. 8, while the list of source parameters, including fault rupture geometry, location of hypocentre, scalar seismic moment and source time function, is provided in Table 3. The source model is characterized by rather shallow asperities, lying at about 6 km depth, which, coupled with the depth of the hypocentre location, may favour updip directivity conditions that may explain the large velocity pulses observed in the Mirandola area.

For the final adjustment of the model, the most significant improvements were obtained (i) by increasing the peak value of the slip distribution from about 50 cm (Pezzo *et al.* 2013) to about 70 cm and (ii) by increasing the dip angle from 40° to 60°. As regards sensitivity to the dip angle, several authors already pointed out the discrepancy between the low values of dip estimated according to the published fault plane solutions of the May 29 earthquake (e.g. Scognamiglio *et al.* 2012; Cesca *et al.* 2013; Pezzo *et al.* 2013), with both the relocated aftershock alignment along a plane dipping about 70° (Govoni *et al.* 2014) and the best-fit source model

Table 3. Fault parameters adopted in the present work.

Fault geometry	Fault parameters	Present Study
	Fault Origin F_O (Lat, Lon)	$(44.900\ N, 10.914\ E)$
	Top Depth of Fault H_{min} (km)	3.7
	Length along Strike L (km)	22
	Width along Dip W (km)	12
	Epicenter (Lat, Lon)	$(44.851\ N, 11.086\ E)$
	Focal Depth (km)	10.4
	Strike $(°)$	95
	Dip $(°)$	60
	Rake $(°)$	90
	Seismic moment M_0 (Nm)	$9.35 \cdot 10^{17}$
	Rise time τ (s)	0.70
	Rupture Velocity V_R (m/s)	$0.85\ V_S$
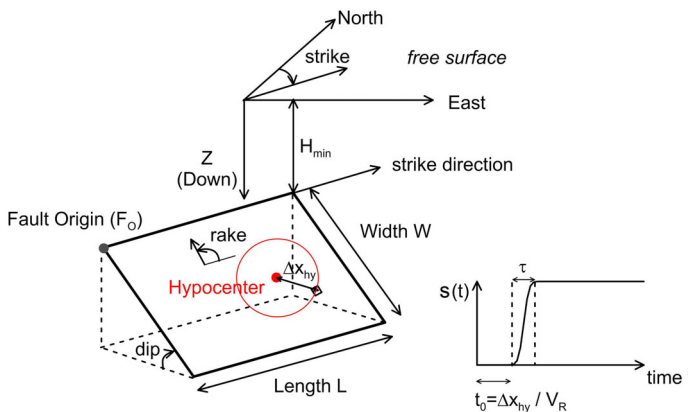
based on finite-element simulations (Tizzani *et al.* 2013), suggesting a listric geometry of the fault, the steepest part of which dips about 65° between 5 and 8 km depth (see their Fig. 3h). To clarify the improvement obtained by a larger dip angle through numerical modeling, we show in Fig. 9 the comparison of NS velocity components at several near-source stations for two different values of the fault dip angle. It can be noted that, in the case of dip = 40° (right-hand side), a good agreement is found for stations MIR01 and SAN0, S of the epicentre. However, moving Northwards, the simulation fails to predict the phases of both MRN and MIR02. A much better agreement is obtained when considering the dip = 60° (left-hand side): in this case, not only the velocity pulse at MRN is captured with a striking detail, but also it is possible to justify the previously noted nearly out-of-phase motion at MIR01 and MRN stations.

Therefore, our results support the interpretation, discussed in detail by Govoni *et al.* (2014), that the May 29 event nucleated along a listric fault having low dip angles in the deeper nucleation region, and becoming steeper in its shallowest part, where the largest amount of energy was released.

Note, at top of Fig. 9, that 1D finite-fault simulation at the MIR08 station, located at about 4 km N of MRN, clearly shows an anticipated trigger of strong motion, while amplitude is reasonably well predicted. This is because the local thickness of the Quaternary sediments (Qm in Fig. 9) is much larger than provided by the model of Table 2. By modifying such thickness for the various recording stations and looking for the best fit with records, we were able to constrain with reasonable detail a model for the base of Quaternary sediments, at least in the near-source region, which was subsequently used to define the seismic velocity structure of the 3D computational model. At MIR08, the best agreement was found for thickness $H = 1$ km, at MIR02 and SAN0 $H = 0.3$ km, at MIR01 $H = 0.2$ km, while the best agreement at MRN was for the model reported in Table 2.

As a final remark, we note that, due to the combination of the shallow asperity distribution shown in Fig. 8 with the relatively low values of seismic velocities of the corresponding crustal region, the rupture velocity turns out to play a key role. Therefore, care

was taken to verify the effect of the possible onset of super-shear conditions. For this purpose, we show in Fig. 10 the simulated NS velocity, obtained in super-shear ($V_R = 2800\ \mathrm{m\,s^{-1}}$) and sub-shear conditions ($V_R = 2200\ \mathrm{m\,s^{-1}}$), compared with the recording at MRN, that is, one of those stations lying in the updip direction of the fault. It is found that, for such updip stations, the super-shear conditions result in unrealistically high peaks of ground motion, so that their potential effect on near-source ground motion during this earthquake was ruled out.

4 THE SPECTRAL ELEMENT CODE SPEED

The software package SPEED (http://speed.mox.polimi.it) is apt to simulate seismic wave propagation at local or regional scale. The code is based on the Discontinuous Galerkin Spectral Element (DGSE) method, a non-conforming version of the classical SE formulation, as explained in Antonietti *et al.* (2012). SPEED was recently applied to study seismic risk scenarios in large urban areas for reinsurance evaluations (Paolucci *et al.* 2014), as well as for the analysis of city–site interaction effects related to the dynamic response of large infrastructures (Mazzieri *et al.* 2013).

The SE method was originally developed in computational fluid dynamics (see Patera 1984) and then successfully adapted to address seismic wave propagation studies (early applications can be found in Seriani *et al.* 1995; Faccioli *et al.* 1997; Komatitsch & Tromp 1999). Nowadays the SE approach is among the most widely used in computational seismology. For a detailed review, the reader may refer to Komatitsch *et al.* (2005) and Chaljub *et al.* (2007) .

The success of the SE method is due to its capability of providing fast and highly accurate solutions (Maday *et al.* 1989) and its easy parallel implementation on large supercomputers (Göddeke *et al.* 2014). To better exploit their intrinsic *h–p* nature, that is, the possibility to employ elements of variable size (*h*) and polynomial approximation degree (*p*), SE methods can be extended to address discontinuous approximations (e.g. Käser & Dumbser 2006; Wilcox *et al.* 2010; Antonietti *et al.* 2012; Peyrusse *et al.* 2014),

Hisada simulation dip 60° - NS

Hisada simulation dip 40° - NS
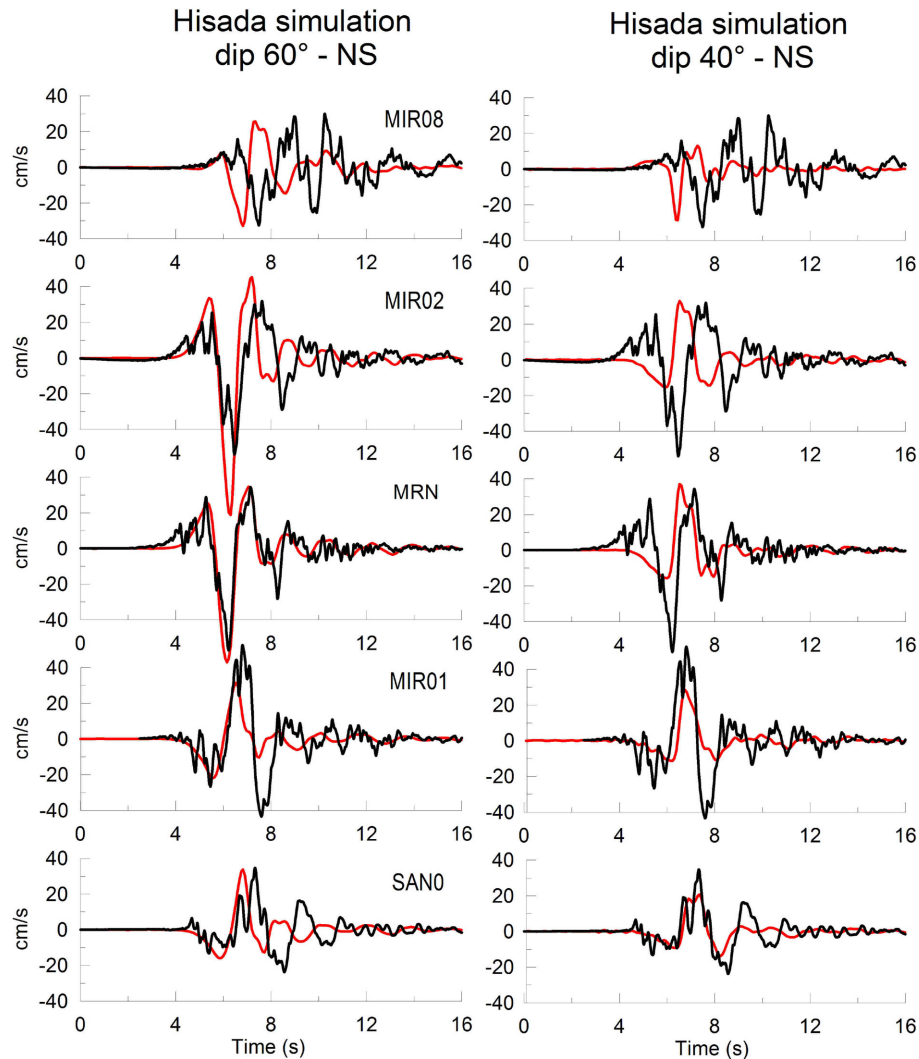
Figure 9. Comparison of NS velocity records (black lines) and numerical (Hisada) results (red lines) obtained using the proposed slip model with fault dip = 60° (left) and dip = 40° (right).
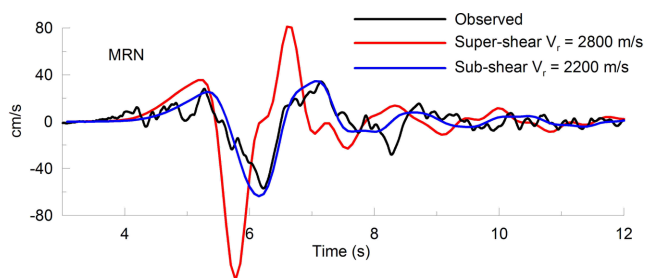
Figure 10. Effect of super-shear ($V_R = 2800\,\mathrm{m\,s^{-1}}$, red line) and sub-shear ($V_R = 2200\,\mathrm{m\,s^{-1}}$, blue line) rupture velocities, on the NS component of velocity at MRN station, using the kinematic model in Fig. 8. The observed velocity time history is shown by the black line.

suitable to capture local variations of the physical solutions. The DGSE approaches have been shown to preserve the same accuracy as SE methods and to feature low dissipation and dispersion errors (see e.g. De Basabe *et al.* 2008; Hesthaven & Warburton 2008; Antonietti *et al.* 2012), so that they guarantee an accurate approximation of amplitudes and phases of the wavefield. On the other hand,

DGSE methods are much more flexible than SE methods, since they can handle subdomainwise non-matching grids and different local approximation degrees, making such schemes well suited for simulations with adaptive choice of discretization parameters. More precisely, the spatial discretization and/or the local polynomial degree can be tailored to the region of interest (e.g. buildings or other civil engineering structures in contact with large-scale soil domains). Furthermore, DGSE methods enjoy a high level of intrinsic parallelism, allowing the application of parallel computations massively (Paolucci *et al.* 2014).

The DGSE method proposed by Mazzieri *et al.* (2013) has been implemented in SPEED, a certified open-source code for the simulation of seismic wave propagation in three-dimensional complex media as well as soil-structure dynamic interaction problems. SPEED is naturally designed for multicore computers or large clusters. It is written in Fortran90 using its pseudo-object oriented features. It takes advantage of the hybrid parallel programming based upon the Message Passing Interface (MPI) library, relying on the domain decomposition paradigm, and the OpenMP library for multithreading operations on shared memory. The mesh generation may be accomplished using a third party software, for example, CUBIT (http://cubit.sandia.gov/) and load balancing is made easier by graph

partitioning based on the METIS library (glaros.dtc.umn.edu/) included in the package.

The present version of SPEED includes the possibility to treat linear and non-linear viscoelastic soil materials, either with frequency proportional quality factor Q (Stupazzini *et al.* 2009), or frequency constant quality factor (Moczo *et al.* 2014). Paraxial boundary conditions (Stacey 1988) reduce spurious reflections from outgoing waves inside the computational domain, while time integration can be performed either by the second-order accurate explicit leap-frog scheme or the fourth-order accurate explicit Runge–Kutta scheme (see Quarteroni *et al.* 2007).

SPEED has been verified in a number of benchmarks (see Mazzieri *et al.* 2013), including the ones proposed by Day & Bradley (2001), and it has been successfully applied to the Grenoble experiment (Chaljub *et al.* 2010), where realistic 3D models of both the source and source-to-site propagation path were addressed. Furthermore, recently the code has been employed to simulate real seismic events, such as the 2009 April 6 L'Aquila (Smerzini & Villani 2012) and the 2011 February 22 Christchurch earthquakes (Guidotti *et al.* 2011).

5 SETUP OF THE 3D NUMERICAL MODEL

The computational domain adopted for the numerical simulation of the M_W 6.0 May 29 earthquake extends over a volume of about 74 $\times$ 51 $\times$ 20 km^3 and is discretized using an unstructured conforming hexahedral mesh with characteristic element size ranging from $\approx$150 m at the surface to $\approx$1500 m at the bottom of the model, see Fig. 11. The mesh was created in order to propagate frequencies up to about 1.5 Hz.

Compared to standard approaches based on plane wave propagation analyses through horizontally layered media, the distinctive features of the numerical model are (see Fig. 11): (i) a kinematic representation for the seismic fault rupture of the 29 May earthquake and (ii) inclusion of a 3D velocity model of the Po Plain,

taking into account the spatial variation of the most relevant geological discontinuities beneath the surface sediments, which have significant effects on the seismic wave propagation. Due to the small topographic variations of the investigated area, a flat-free surface has been used, even though SE methods are naturally suited to deal also with surface topography variations.

The adjustment of the kinematic fault model parameters was already introduced and discussed in Section 3, and the resulting model illustrated in Fig. 8 and Table 3. Note that, in the 3D simulations, we enhanced the slip distribution by making it compatible with a k^{-2} model, using the approach developed by Herrero & Bernard (1994), in order to improve the high-frequency radiation from the seismic source. The source time history $s(t)$ is given by an approximate step function, as follows:

$$s(t) = 1/2 \cdot \left[1 + \mathrm{erf}\left(4 \cdot \frac{t - 2\tau}{\tau} \right) \right]$$

where $\mathrm{erf}(\cdot)$ is the error function and $\tau = 0.7$ s is rise time, assumed to be constant across the fault plane. As previously discussed, to avoid unrealistically high-velocity pulses due to super-shear effects (see Fig. 10), the rupture velocity was bounded to $V_R = 0.85 V_S$, being V_S the shear wave velocity at the corresponding source depth.

To construct the 3D seismic velocity model, two main geological interfaces were considered. First, the base of Quaternary sediments (z_Q), was estimated from the geological cross-sections available within the study area (see e.g. the bottom panel of Fig. 1), combined with the quantitative evaluation of sediment thickness at several selected stations to provide the best fit on near-source records, as mentioned in Section 3. Note that we considered 0.15 km $< z_Q$ < 2 km throughout the model. Second, the base of Pliocene formations (z_P), was derived from the structural map of Italy (Bigi *et al.* 1992, see shaded tones in Fig. 1, top panel) and made available as a georeferenced image by Burrato (INGV, personal communication, 2012). Modeling the variability of the Quaternary sediments thickness throughout a small spatial range around Mirandola, was found to play a key role to simulate with reasonable accuracy the prominent trains of surface waves observed along the MIR array.
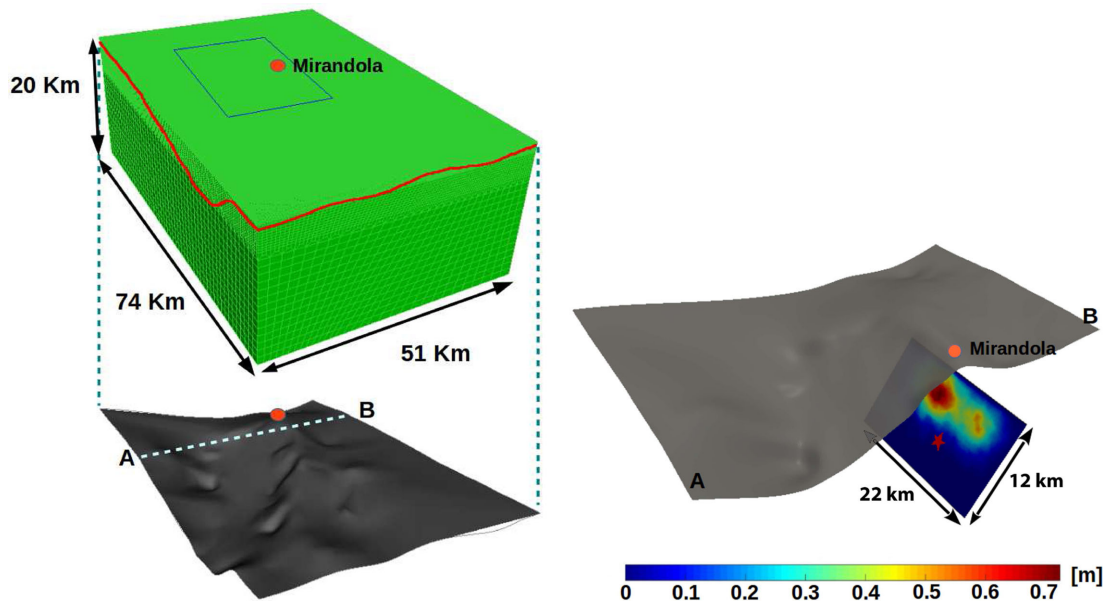

Figure 11. Left: 3D numerical model including the seismic fault responsible of the M_W 6.0 May 29 earthquake and the buried topography, corresponding to top of the Miocene formations (denoted by M in Fig. 1). Right: assumed slip distribution to model the earthquake fault rupture, as described in Section 3 and illustrated in Fig. 8.

Table 4. Dynamic properties of the geological formations in the 3D numerical model. z_Q and z_P denote the base of Quaternary (Q_M in Fig. 1) and Pliocene ($M\text{-}P_1$ in Fig. 1) soil units. Q_S is defined at the reference frequency $f_0 = 0.67$ Hz.

Geological unit	Depth z (m)	ρ (kg m^{-3})	V_S (m s^{-1})	V_P (m s^{-1})	Q_S ($-$)
Quaternary	$z < 150$	1800	300	1500	30
	$150 < z < z_Q$	$1800 + 6\sqrt{z - 150}$	$300 + 10\sqrt{z - 150}$	$1500 + 10\sqrt{z - 150}$	$V_S(z)/10$
Pliocene	$z_Q < z < z_P$	$2100 + 4\sqrt{z - z_Q}$	$800 + 15\sqrt{z - z_Q}$	$2000 + 15\sqrt{z - z_Q}$	$V_S(z)/10$
Before Pliocene	$z > z_P$	See seismic model in Table 2 at corresponding depth			

Table 5. Walltime for a single simulation of the Emilia earthquake, performed both on Fermi (CINECA) and Idra (MOX) clusters.

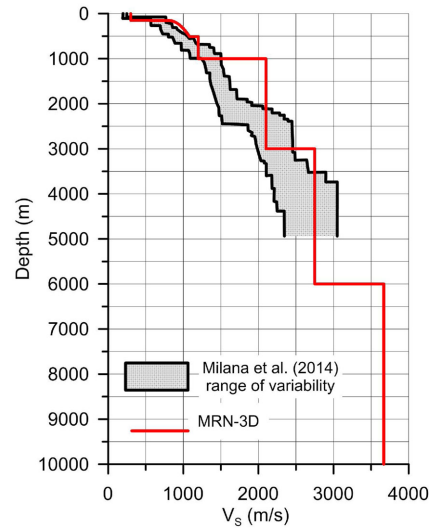| Cluster	Cores	Walltime (h)
Fermi (CINECA)	4096	4.98
Idra (MOX)	72	19.83
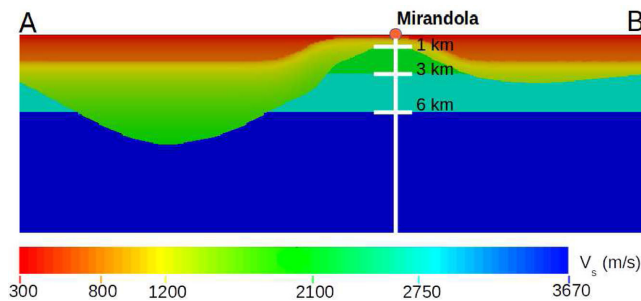
Figure 12. Representative NS cross-section of the numerical model passing through Mirandola, showing the V_S model adopted in the 3D numerical simulations for both Quaternary-Pliocene deposits and bedrock older formations.


Figure 13. Comparison between the V_S profile implemented in the 3D numerical simulations and the 1D average best model proposed by Milana *et al.* (2014) for the Mirandola area.

Based on the formulae adopted in Table 4, V_S in the Quaternary sediments varies from 300 to 730 m s^{-1}, while in the Pliocene layers it varies from 800 to about 1850 m s^{-1}, the latter value being associated to the maximum depth of the Pliocene, around 7.5 km. Average values of Poisson ratio ν are 0.45 in the Quaternary sediments and 0.29 in the Pliocene formations. A representative NS cross-section of the V_S model, passing through Mirandola, is illustrated in Fig. 12. A linear viscoelastic soil model with frequency proportional Q factor has been assumed in these simulations (see Stupazzini *et al.* 2009).

It should be remarked that the resulting 3D numerical model is a compromise between, on one side, the need to fit as closely as possible the available geological and geophysical information throughout a large spatial region, and, on the other side, to cast such information within a reasonably simple form apt to construct the computational model. Note that, to reduce the number of degrees of freedom in the numerical grid, we had to constrain the shear wave velocity in the top layer to a minimum value of 300 m s^{-1}.

In spite of such approximations, the numerical model is in reasonable agreement with previously published studies. Namely, we made reference to several 1D profiles available in the Mirandola area (Martelli & Molinari 2008; DPC-INGV Project S2 2012; Milana *et al.* 2014), as well as with the recent work published by Molinari *et al.* (2015), who calibrated a 3D seismic model for the Po Plain and used it for spectral elements numerical simulations on a much broader area than considered in this paper, albeit with a much lower frequency resolution ($f < 0.33$ Hz). A comparison of the V_S profile at Mirandola based on our numerical model and the inversion published by Milana *et al.* (2014) is shown in Fig. 13. There is an overall good agreement, except for the $1 - 2$ km depth range, where our values are significantly larger than those of Milana

et al. (2014). However, we verified that such disagreement has only a minor influence on the numerical results.

Finally, the seismic velocity model was implemented into a numerical spectral element model. Considering a rule of thumb of four gridpoints per minimum wavelength for non-dispersive wave propagation in heterogeneous media by the SE approach (Faccioli *et al.* 1997), and considering a maximum frequency $f_{\max} = 1.5$ Hz, the model consists of $1'975'240$ spectral elements, resulting in approximately 150×10^6 degrees of freedom, using a third-order polynomial approximation degree. The time integration has been carried out with the leap-frog scheme, choosing a time step equal to 0.001 s for a total observation time $T = 30$ s. The simulations have been performed both on the Idra cluster located at MOX-Laboratory for Modeling and Scientific Computing, Department of Mathematics, Politecnico di Milano (http://hpc.mox.polimi.it/hardware/) and on the Fermi cluster located at CINECA, Bologna, Italy (http://www.hpc.cineca.it/). As an indicator of the parallel performance of the code SPEED, we report in Table 5 the total simulation time (walltime) for a single run of the Emila earthquake, considering both Fermi and Idra clusters.

6 NUMERICAL RESULTS AND COMPARISON WITH RECORDS

Physics-based numerical simulations have the power to provide a complete picture of ground motion, including its spatial variability on a wide scale, that cannot be achieved by any other approach for earthquake ground motion prediction. As an example, in Fig. 14 several snapshots are shown representing the horizontal (FN) velocity wavefield on a NS cross-section passing through the Mirandola anticline along the MIR array (see strong-motion stations MIR01,
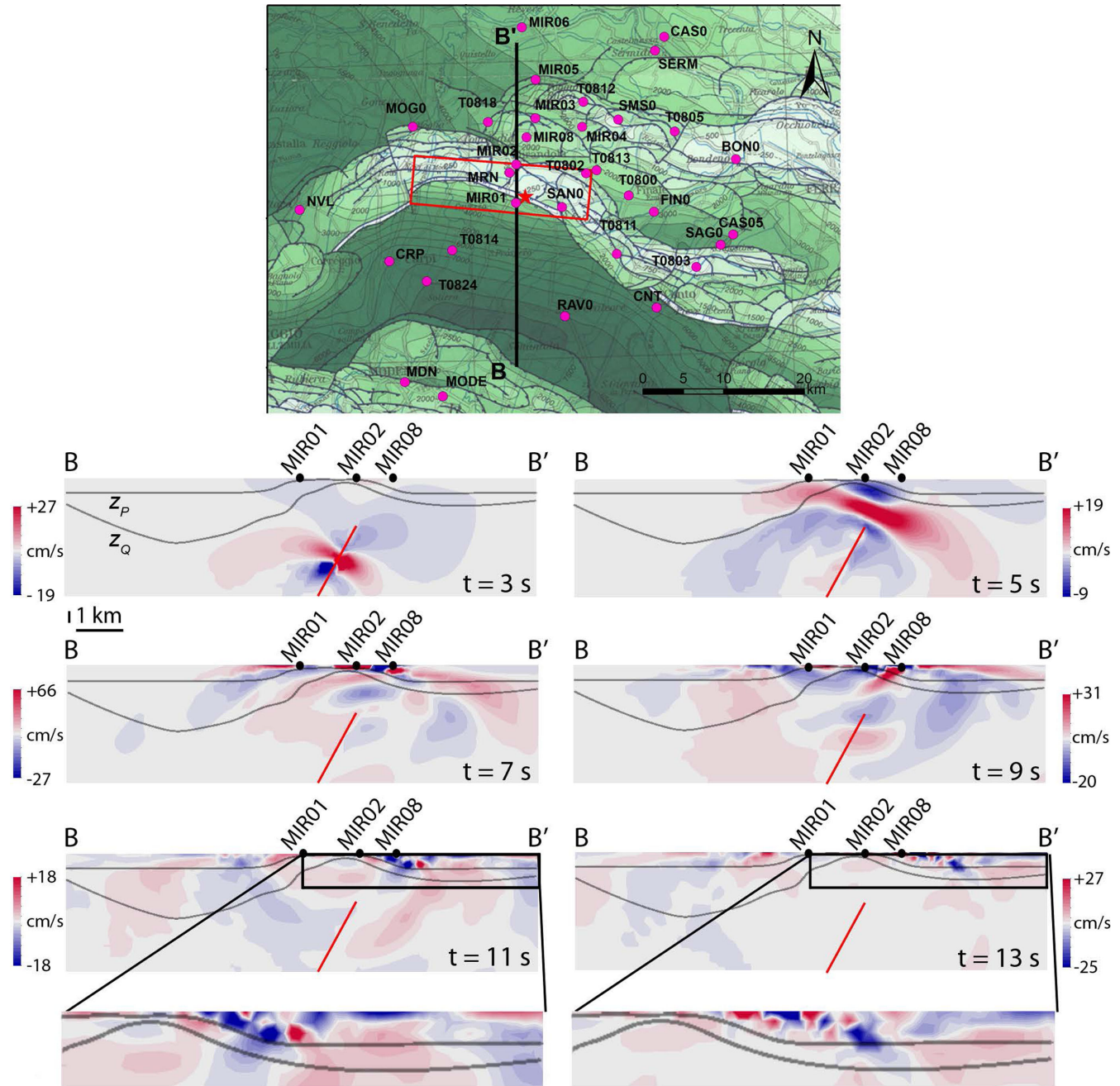
Figure 14. Snapshots of the horizontal (FN) velocity wavefield across a NS cross-section passing through the Mirandola high; note the different scales of the plots. The general location of the cross-section together with the surface projection of the fault plane is shown in the top map.

MIR02 and MIR08, as indicated on the map). The snapshots high-light the predominant role played by the updip source directivity coupled with the irregularity of the buried bedrock configuration, leading, on one side, to the largest velocity peaks at the updip stations, and, on the other side, to the generation of trains of sur-face waves propagating from both N and S sides of the Mirandola high, but with largest peaks in the N direction, as a consequence of the updip directivity. The zoom of the velocity field within the top Northern portion of the cross-section (bottom side of Fig. 14) allows one to point out also the dispersive features of surface wave prop-agation, with long-period/wavelength components travelling faster away from the source than the short period ones.

After having highlighted through the previous figure some gen-eral features of the seismic wave propagation problem, we aim now at illustrating in more detail the results of the numerical simula-tions and at comparing them with SM records. Specifically, we show in Fig. 15 the three-component velocity waveforms and in Fig. 16 the corresponding Fourier amplitude spectra (FAS) at 10 representative SM stations. The latter were chosen to provide a relatively uniform sample in terms of their geographic distribu-tion. Both recorded and simulated waveforms were band-pass fil-tered with an acausal Butterworth third-order filter between 0.1 and 1.5 Hz, the latter being the frequency resolution of the numerical model.
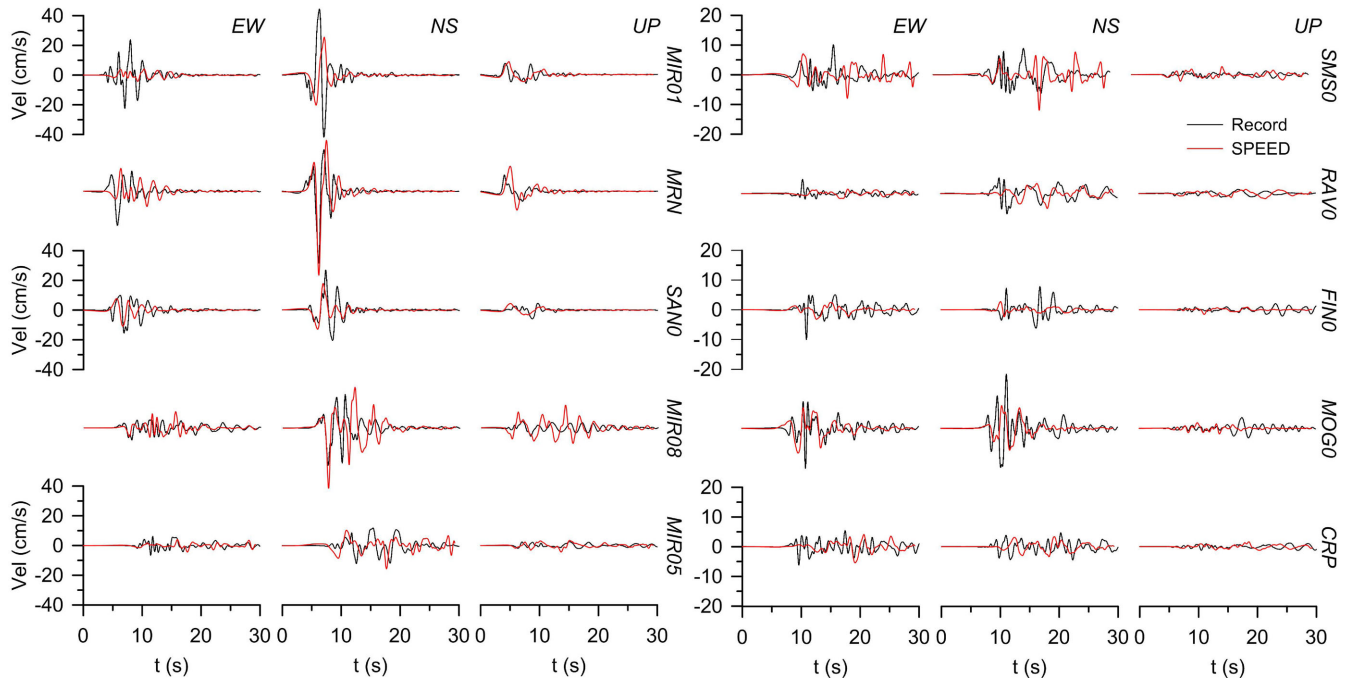
Figure 15. Comparison between recorded (black line) and simulated (red line) three-component velocity waveforms for a representative subset of 10 SM stations. Data are band-pass filtered between 0.1 and 1.5 Hz.
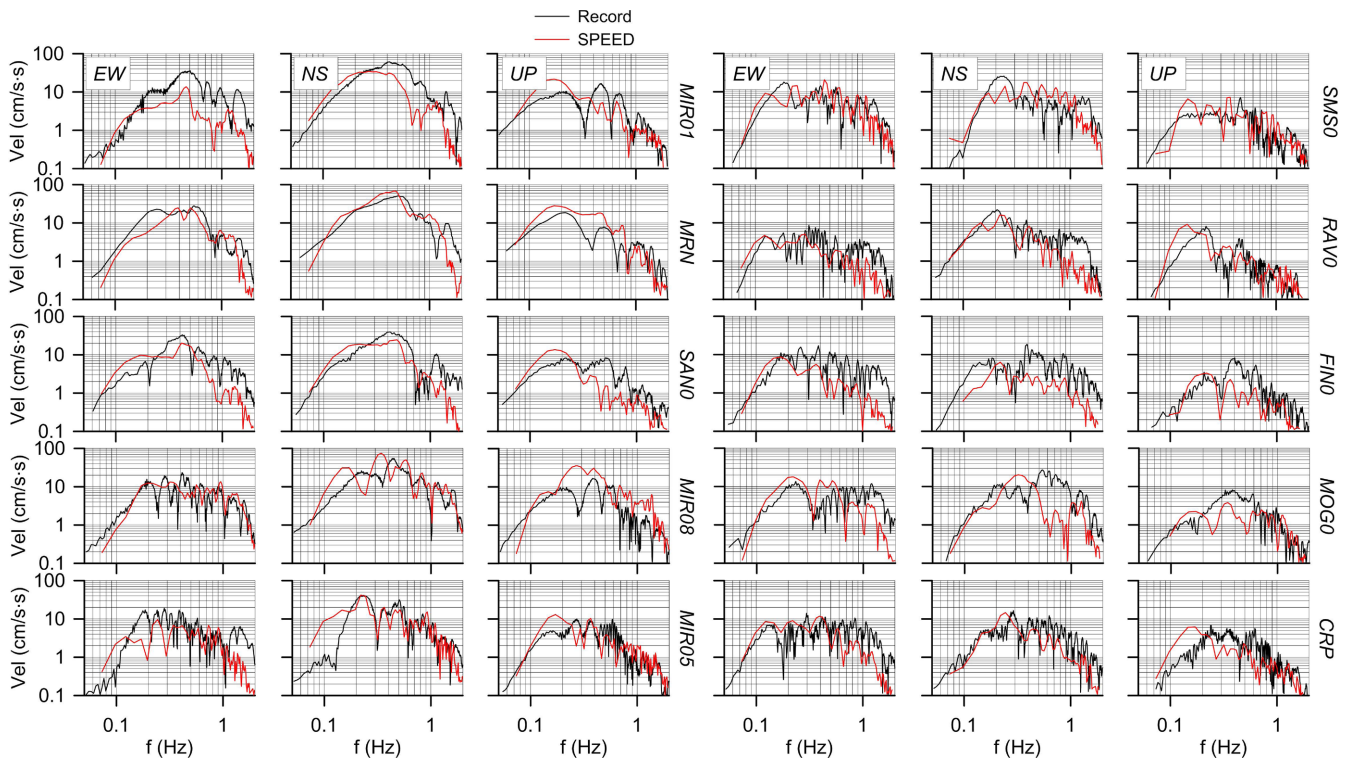
Figure 16. As in Fig. 15 but in terms of Fourier amplitude spectra (FAS) of velocity signals.

On the whole, the agreement between synthetics and records is good in both time and frequency domain, especially on the horizontal NS and vertical component for almost all considered stations. In particular, the agreement of the NS velocity pulse, with PGV around 50 cm s^{-1} at the closest stations to the epicentre (i.e. MRN and MIR01) is remarkable and proves the effect of updip directivity from the slip distribution model established in Section 3. Referring

to the comparison in terms of Fourier spectra, it turns out that, in general, there is a satisfactory agreement between simulated and recorded amplitudes for frequencies up to about 1 Hz, although synthetic tends to underpredict the observed amplitudes. While leaving to the following section some comments on the prediction of the vertical components of motion, which is also satisfactory, we note that we did not succeed to obtain a similar good agreement on
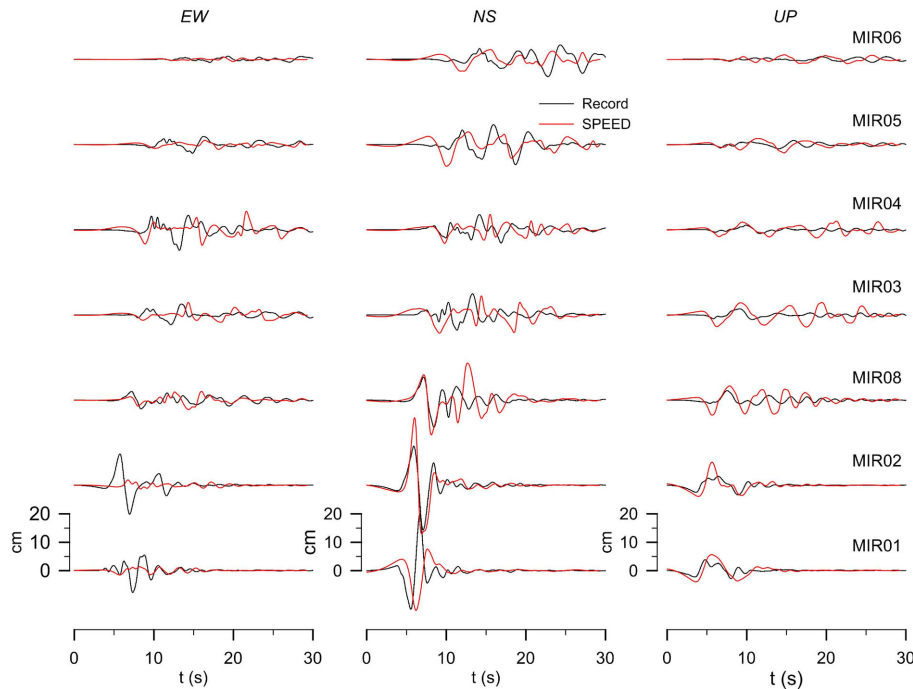
Figure 17. Comparison between recorded (black line) and simulated (red line) three-component displacement waveforms along the MIR transect. Data are band-pass filtered between 0.1 and 1.5 Hz.

the EW component, especially at those stations located at short epicentral distances ($R_e < 5$ km), such as MRN and MIR01, while the comparison improves at other stations. This is probably due to the insufficient complexity both of the seismic fault and of the geological model, the latter consisting of a pretty regular ridge elongated roughly EW. In such conditions, because of a nearly symmetric configuration of both the slip distribution and of the 3D numerical model in the epicentral area, the simulated EW components, especially along the MIR transect, roughly oriented NS, turn out to be negligible, contrary to the observational evidence.

The analysis of ground motion along the MIR transect is particularly meaningful and it is shown in Fig. 17, where the recorded and simulated three-component displacement time histories in the frequency range 0.1–1.5 Hz along such transect are compared, with the exception of station MIR07, which falls out of the numerical model. It is found that numerical simulations provide a reasonably good prediction of one of the most significant features shown by the May 29 SM data set, that is, the onset of a train of Northwards propagating surface waves, generated by the buried morphological irregularity of the Mirandola structural high (see sketch in Fig. 6). In the epicentral region, body and surface waves overlap, while the latter become predominant at distances larger than about 10 km, as highlighted by the long-period components in the coda of the signals. As remarked previously, EW components at these close-by stations are poorly predicted. Similar conclusions on the role of the buried morphology on the onset of surface waves during the Po Plain earthquakes were recently pointed out by Molinari *et al.* (2015), the numerical results of which however were limited to the period range $T > 5$ s and far away from the seismic source. The overall performance of the numerical simulations was evaluated in a quantitative way using the GoF criteria proposed by Anderson (2004). For the frequency band of interest (i.e. 0.1–1.5 Hz), a GoF score from 0 to 10 (<4, poor; 4–6, fair; 6–8, good; ≥8, excellent) is estimated on five metrics of interest for engineering purposes, namely: energy

duration (ED), PGV, PGD, RS acceleration and FAS. Note that FAS and RS criteria are evaluated considering only the frequencies and structural periods within the range 0.1–1.5 Hz of validity of the numerical simulations. The GoF scores, computed for each criteria and for the three components of motion, are shown in Fig. 18 for the same subset of 10 SM stations as considered in Figs 15 and 16. These results confirm that:

(1) With few exceptions, the numerical model provides predictions that are in overall good agreement (from fair to excellent) with the SM records.

(2) Results for the NS component are significant better than those for other components. With the exception of stations FIN0 and MOG0, the average GoF scores are in the range from good to excellent.

(3) Results for the EW and vertical components have an average GoF score from fair to good and show a larger scatter among the considered criteria.

Following Olsen & Mayhew (2010), who proposed to compute final GoF estimates as weighted average of selected metrics, we adopted a standard equal weighting for the fives metrics under consideration to compute the average GoF value for each ground motion component. Fig. 19 presents an overview of the misfit between records and simulated results at territorial scale, showing the average GoF scores for the EW (top, left), NS (top, right) and vertical (bottom) components at all available SM stations at $R_e < 30$ km. It is found that for the majority of stations the agreement between simulations and observations is from fair to good, with best results on the NS component, as already noted previously. A poor agreement is found at some sites but it is relevant to underline that average scores below 4 are never determined simultaneously on all components (apart from station CAS05 showing unusual large amplitude waves in the coda of the signal).
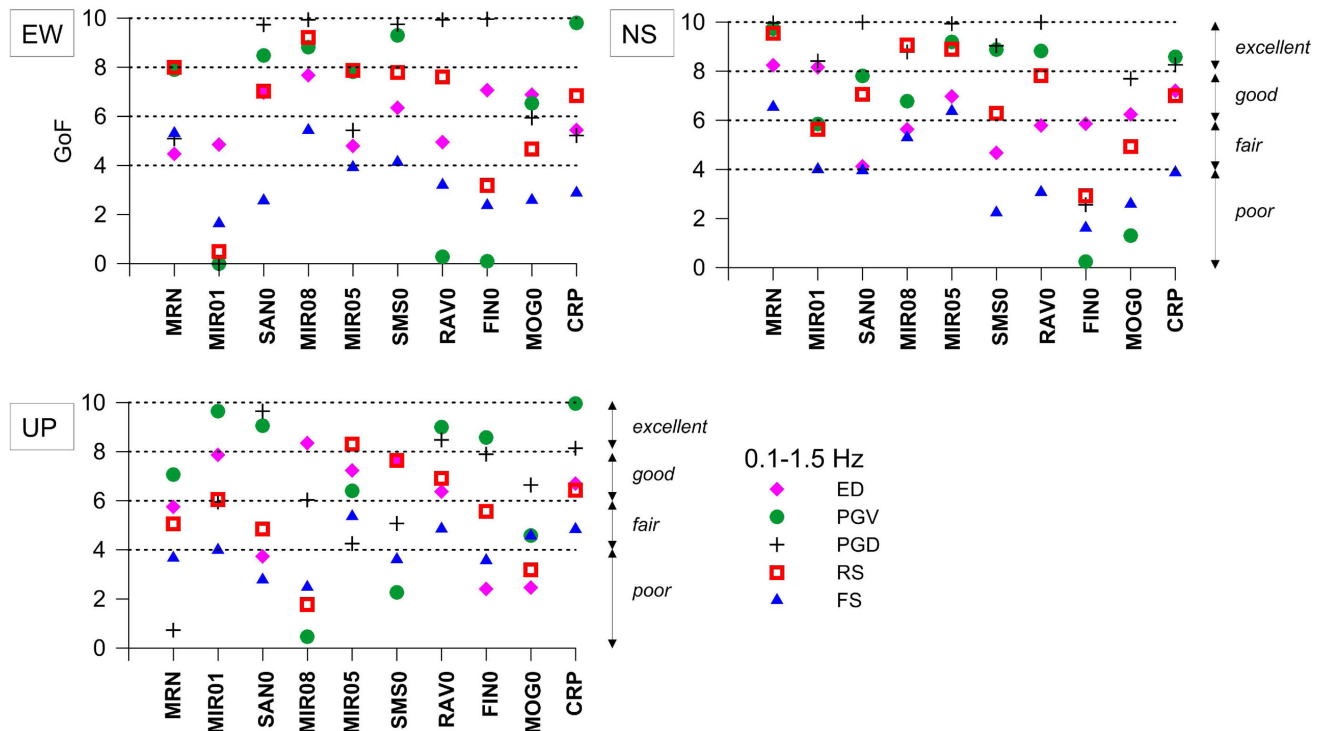
Figure 18. Goodness of fit (GoF) scores evaluated according to Anderson (2004) at 10 SM stations for five criteria, energy duration (ED), peak ground velocity (PGV), peak ground displacement (PGD), response spectra (RS) and Fourier spectra (FS), and for the three components of motions (horizontal EW and NS, top panel; vertical, bottom panel).

7 PREDICTION OF EARTHQUAKE-INDUCED GROUND UPLIFT

As a key benchmark to assess the accuracy of the proposed fault model and the performance of the numerical simulations at very low frequencies, we address in this section the comparison of the numerical results with the ground deformation maps produced starting from the aftermath of the May 20 main shock (Salvi *et al.* 2012; Pezzo *et al.* 2013), taking advantage of the Synthetic Aperture Radar Interferometry (InSAR) survey activated by the Italian Space Agency, with the coverage of all four Constellation of Small Satellites for the Mediterranean Basin Observation satellites (COSMO-SkyMed). In Fig. 20 (right-hand side), the corrected COSMO-SkyMed map is shown, providing detailed measures of ground uplift during the May 29 earthquake, with maximum values slightly exceeding 10 cm within the epicentral area. On the left-hand side of the same figure, the numerical simulations results are also shown. These are computed by the values of the simulated unfiltered vertical displacements, averaged over the last 5 s of the simulation, after ground shaking has ended. A remarkable agreement is found, except for a slight underprediction of uplift in the Western side of the fault area.

As a further verification of the fit of the numerical simulations to the observations, the simulated vertical displacement time histories were compared with displacement records obtained by double integration of accelerations. To avoid losing the information of permanent displacement by high-pass filtering, uncorrected acceleration records were simply processed through a piecewise baseline correction, applied on the velocity trace. Further details on such processing can be found in Maini (2015). Results, illustrated in Fig. 21, confirm, on one side, that the baseline processing was successful in reproducing permanent ground

deformations close to those inferred from InSAR processing, and, on the other side, the good performance of the numerical model.

8 GROUND SHAKING AND I_{MCS} MAPS

As a final comparison between simulations and observations, Fig. 22 (left panel) illustrates the spatial distribution of *PGV* (*gmh* = geometric mean of horizontal components), as predicted by our physics-based 3D numerical simulations. For comparison, the observed *gmh* values of *PGV*, obtained at the available SM stations in the same frequency range of 3D numerical simulations, are depicted by filled dots. The simulated ground shaking map shows a characteristic two-lobed pattern (as highlighted within the superimposed box), with maximum amplitudes concentrated within two regions, W and E of the main shock epicentre. Maximum *gmh PGV* values of about 60 cm s^{-1} are found, in agreement with ground motion recordings. The comparison with the available SM data points out that the overall spatial distribution of simulated ground motion matches reasonably well the recorded one. Note that, to produce the map in Fig. 22, both numerical results and records have been low-pass filtered at 1.5 Hz, for consistency with the spatial resolution of the numerical mesh. However, the effect of such filter on *PGV* is limited, while it was not possible to produce a similar map in terms of *PGA*.

It is worth noting that the two-lobed pattern of gmh *PGV* turns out to be fairly consistent with the spatial distribution of macroseismic intensity, I_{MCS}, depicted in Fig. 22, on the right panel. The map was generated by spatial interpolation of the I_{MCS} data, as provided by the DPC macroseismic survey (Galli *et al.* 2012), using the spline with barriers method implemented in ArcGIS (http://www.arcgis.com). This shows the largest concentration of damage in two NS-elongated areas, one passing through Cavezzo and Mirandola, west of the
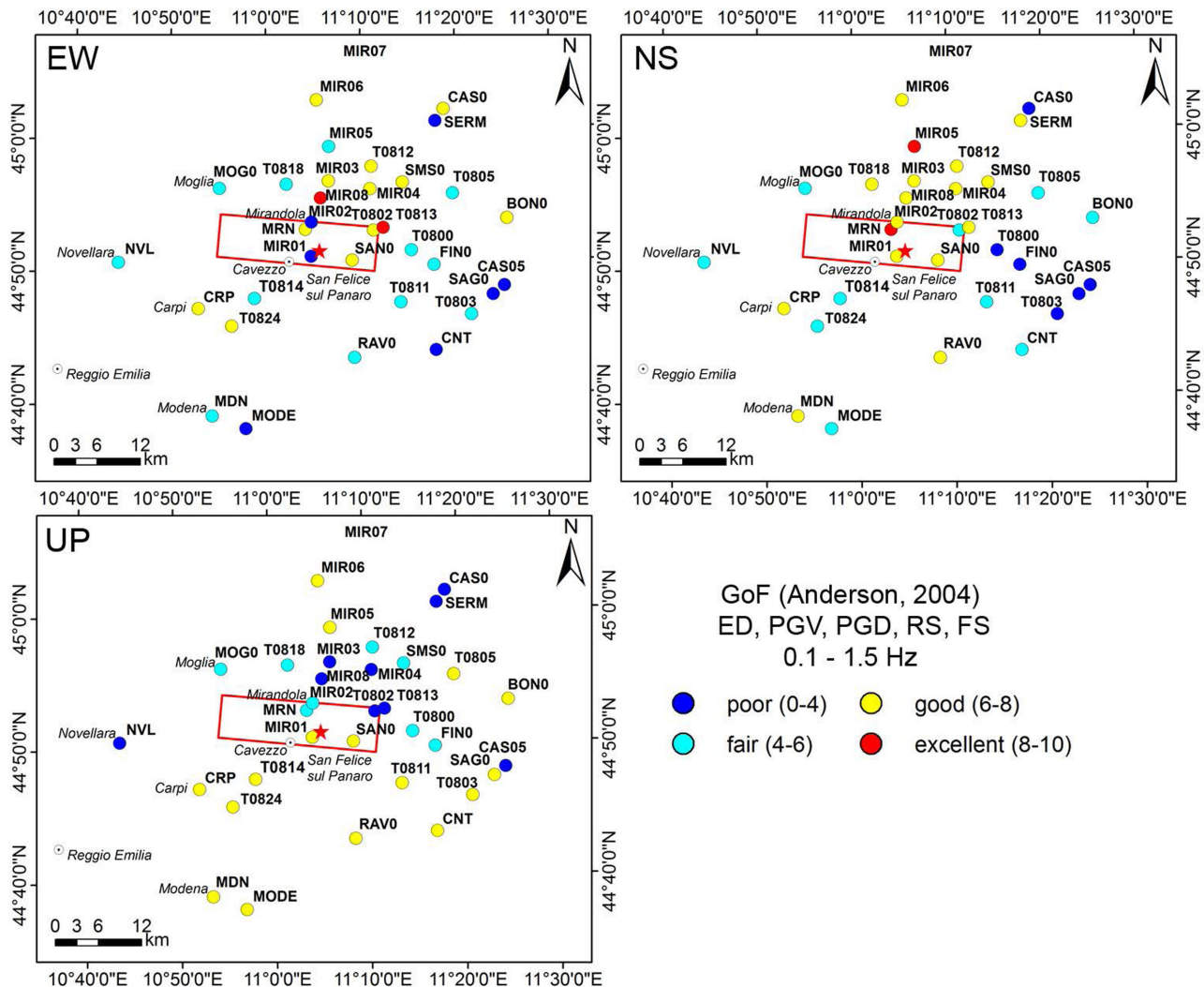
Figure 19. Map of GoF scores for all available SM stations at $R_e < 30$ km for EW, NS and vertical components.

epicentre, and the second passing through San Felice sul Panaro, east of the epicentre. Note that the I_{MCS} map shows the combined effects of the entire seismic sequence from 2012 May 20 to June 3. This is the reason why, rather surprisingly, the heaviest damage occurred in the small area west of Mirandola, in the municipality of Novi di Modena. As a matter of fact, the last shock of June 3, M_L 5.1, acted on buildings slightly damaged by the previous shocks, but which could not withstand the very last one. Therefore, although the cumulative effects of the sequence prevent an accurate discrimination of the impact of the May 29 earthquake alone, the area mostly affected by this earthquake can be roughly included within the dashed quadrangular box in Fig. 22. The similarity of the two-lobed patterns of both the *PGV* and of the I_{MCS} map is worth to be noted, and it may confirm that the pronounced spatial variability of the distribution of damage is likely to be strongly related to the focal mechanism of the earthquake, rather than to amplification effects associated to local site conditions, which are fairly homogeneous throughout the epicentral area.

9 CONCLUDING REMARKS

3D physics-based numerical simulations of earthquake ground motions are deemed to become soon the main and more reliable tool to produce realistic scenarios of future earthquakes. This is expected to have a deep impact in terms of creation of earthquake scenarios for seismic risk analyses in large urban areas or for critical structures and infrastructures. Also, this is expected to provide the key to improved predictions of ground motion, and better constrained seismic hazard assessment (Villani *et al.* 2014), in those conditions that are poorly covered by available worldwide records, such as near-source locations coupled with complex shallow geology.

Several research groups worldwide have developed numerical codes suitable to perform such simulations, which typically require high-performance computing tools, so that the number of applications for earthquake ground motion predictions in different parts of the world is ever growing, as shown by the selection of studies carried out in the past 10 yr in Table 6. However, for the use of such tools to be accepted in the engineering world, the frequency range of the analyses (f_{max}) must be as large as possible to encompass the seismic response of different types of structures. As shown in Table 6, there is a tendency of increasing f_{max} in the last few years, but still few applications go beyond 1 Hz. Besides computational constraints, extending f_{max} requires the seismic source to be complex enough to radiate a sufficiently wide frequency spectrum, as well as the geological model to be detailed enough to capture reasonably well the complexity of real configurations. And, last but not

Figure 20. Map of permanent ground uplift simulated by SPEED (left) and observed by COSMO-SkyMed InSAR processing (right). In both maps the surface projection of the fault area is shown, together with the intersection of the fault plane with ground surface (dashed line).

Figure 21. Comparison between observed (blue line) and simulated (red line) vertical displacement time histories at two near-source recording stations (left, SAN0; right, MRN). Acceleration records were processed by a piecewise baseline correction, suitable to recover permanent displacements.

least, such numerical tools need to be validated against near-source records from real earthquakes, proving therefore their accuracy in those conditions that are mostly relevant for the engineering applications.

The M_W 6.0 2012 May 29 Po Plain earthquake, treated in this work, appeared to be one of the most useful case studies for this purpose, not only because of the availability of a very large number of near-source records, but also because the subsoil conditions of the Po Plain are rather well known, so that construction of a 3D numerical model including its complex buried morphology was possible with a relatively small effort.

A good agreement with records was obtained by adjusting, on one side, the kinematic fault model, with best results obtained for a dip angle of $60°$ and the largest rupture asperities at about 6 km depth with a maximum slip of around 70 cm. On the other side, it was necessary to carefully tune the rapidly varying thickness of Quaternary sediments in the epicentral area, based on the arrival time of the observed waveforms.

Eventually, some important features of the observed near-source earthquake ground motion were accurately reproduced, such as (i) the large FN velocity peaks at the updip stations, (ii) the striking

Figure 22. Left: spatial distribution of *PGV* (*gmh* = geometric mean of horizontal components) from physics-based 3D numerical simulations. The observed values of *gmh PGV* (see filled dots), obtained at the available SM stations, are also superimposed for comparison purposes. Right: I_{MCS} map for the whole 2012 May and June seismic sequence. The superimposed box on both panels denotes the region that is mostly associated to the May 29 earthquake.

Table 6. Selection of recent studies to produce physics-based earthquake ground shaking scenarios in large metropolitan areas. FD = Finite differences; FE = Finite elements; SE = Spectral elements; FV = Finite volume; ADER-DG = High-order Discontinuous Galerkin (Käser & Dumbser 2006).

Reference	Study area	Method	Model size (km)	f_{max}	Scenarios
Aagaard *et al.* (2004)	Taiwan	FE	$160 \times 80 \times 40$	0.5	10
Graves & Wald (2004)	San Bernardino, US	FD	$116 \times 162 \times 50$	0.6	3
Komatitsch *et al.* (2004)	Los Angeles, US	SE	$516 \times 507 \times 60$	0.5	2
Asano *et al.* (2005)	Denali fault sys, Alaska	FD	$480 \times 360 \times 42$	0.5	1
Ewald *et al.* (2006)	Lower Rhine	FD	$140 \times 140 \times 30$	1	4
Olsen *et al.* (2006, 2008)	Southern California, US	FD	$600 \times 300 \times 80$	0.5	3
Furumura & Hayakawa (2007)	Kanto basin, Japan	FD	$440 \times 250 \times 160$	1	1
Day *et al.* (2008)	Southern California, US	FD-FE	$100 \times 100 \times 30$	0.5	60
Wang *et al.* (2008)	Los Angeles, US	FD	$96 \times 87 \times 25.5$	0.56	24
Lee *et al.* (2008a)	Tapei, Taiwan	SE	$102 \times 88 \times 106$	1	10
Lee *et al.* (2008b)	Tapei, Taiwan	FD	$27.8 \times 27.8 \times 3.7$	3	3
Graves (2008)	San Bernardino, US	FD	$65 \times 74 \times 25$	1	1
Rodgers *et al.* (2008)	San Francisco Bay, US	FD	$360 \times 180 \times 50$	0.25	12
Olsen *et al.* (2009)	Southern California, US	FD	N/A	0.5	7
Stupazzini *et al.* (2009)	Grenoble, France	SE	$40.7 \times 50 \times 8$	2	18
Koketsu *et al.* (2009)	Kanto basin, Japan	FD	$154 \times 154 \times 38$	0.5	1
Aagaard *et al.* (2010)	San Francisco Bay, US	FE/FD	$200–220 \times 120–280 \times 36–45$	0.5–1.0	39
Bielak *et al.* (2010)	Southern California, US	FD/FE	$500–600 \times 250–300 \times 50–84$	0.5	3
Gallovič *et al.* (2010)	Parkfield, US	FV/ADER-DG	$100 \times 60 \times 28$	1	6
Graves *et al.* (2011)	Southern California, US	FD	N/A	0.5	840,000
Smerzini *et al.* (2011)	Gubbio, Italy	SE	$62 \times 85 \times 10$	2.5	3
Smerzini & Villani (2012)	L'Aquila, Italy	SE	$62 \times 63 \times 17.7$	2.5	32
Villani *et al.* (2014)	Sulmona, Italy	SE	$48 \times 40 \times 15$	2	91
Roten *et al.* (2011); Roten *et al.* (2012)	Salt Lake basin, US	FD	$60 \times 45 \times 30$	1	6
Molnar *et al.* (2014)	Vancouver region, Canada	FD	$150 \times 180 \times 25$	0.5	8
Taborda & Bielak (2014)	Southern California, US	FE	$180 \times 135 \times 62$	4	3

out-of-phase motion at the close-by stations MIR01 and MIR02, (iii) the pronounced buried topography-induced surface wave trains propagating Northwards and dominating ground motion already at some 10 km distance from the epicentre, (iv) the map of ground uplift on the hangingwall of the fault, (v) the two-lobed pattern of I_{MCS} intensities, well correlated with the *PGV* map from numerical simulations.

A sensitivity study with respect to the "basic" assumptions of linear viscoelastic materials presented in this work, namely: (1) different assumptions of the frequency dependence of the quality factor, *Q*; (2) the non-linear modeling of the seismic response of shallow soft soil sediments; (3) the spatially correlated random source parameters, for the high-frequency content of the seismic radiation to be enhanced; (4) the influence of the seismic velocity model.

REFERENCES

Aagaard, B.T., Hall John, F. & Heaton, T.H., 2004. Effects of fault dip and slip rake angles on near-source ground motions: why rupture directivity was minimal in the 1999 Chi-Chi, Taiwan, earthquake, *Bull. seism. Soc. Am.,* **94**(1), 155–170.

Aagaard, B.T. *et al.*, 2010. Ground-motion modeling of hayward fault scenario earthquakes, Part II: Simulation of long-period and broadband ground motions, *Bull. seism. Soc. Am.,* **100**(6), 2945–2977.

Ambraseys, N. & Douglas, J., 2003. Near-field horizontal and vertical earthquake ground motions, *Soil Dyn. Earthq. Eng.,* **23**, 1–18.

Anderson, J.G., 2004. Quantitative measure of the goodness-of-fit of synthetic seismograms, in *Proceedings of the 13th World Conference on Earthquake Engineering,* 2004 August 16, Vancouver, British Columbia, Canada, Paper No. 243.

Antonietti, P.F., Mazzieri, I., Quarteroni, A. & Rapetti, F., 2012. Nonconforming high order approximations of the elastodynamics equation, *Comput. Method Appl. Mech. Eng.,* **209–212**(0), 212–238.

Asano, K., Iwata, T. & Irikura, K., 2005. Estimation of source rupture process and strong ground motion simulation of the 2002 Denali, Alaska, earthquake, *Bull. seism. Soc. Am.,* **95**(5), 1701–1715.

Bielak, J. *et al.*, 2010. The ShakeOut earthquake scenario: verification of three simulation sets, *Geophys. J. Int.,* **180**(1), 375–404.

Bigi, G. *et al.*, 1992. *Structural Model of Italy 1:500,000,* CNR Progetto Finalizzato Geodinamica.

Bindi, D., Massa, M., Luzi, L., Ameri, G., Pacor, F., Puglia, R. & Augliera, P., 2014. Pan-European ground-motion prediction equations for the average horizontal component of PGA, PGV, and 5 to 3.0 s using the RESORCE dataset, *Bull. Earthq. Eng.,* **12**(1), 391–430.

Boccaletti, M., Bonini, M., Corti, G., Gasperini, P., Martelli, L., Piccardi, L., Severi, P. & Vannucci, G., 2004. *Seismotectonic map of the Emilia-Romagna Region, Emilia-Romagna Region—SGSS and CNR-IGG,* S.EL.CA Florence.

Boccaletti, M., Corti, G. & Martelli, L., 2010. Recent and active tectonics of the external zone of the Northern Apennines (Italy), *Int. J. Earth Sci.,* **100,** 1331–1348.

Bordoni, P. *et al.*, 2012. Preliminary results from EMERSITO, a rapid response network for site-effect studies, *Ann. Geophys.,* **55**(4), doi:10.4401/ag-6153.

Burrato, P., Vannoli, P., Fracassi, U., Basili, R. & Valensise, G., 2012. Is blind faulting truly invisible? Tectonic-controlled drainage evolution in the epicentral area of the May 2012, Emilia-Romagna earthquake sequence (Northern Italy), *Ann. Geophys.,* **55**(4), doi:10.4401/ag-6182.

Cassano, E., Anelli, L., Fichera, R. & Cappelli, V., 1986. Pianura Padana. Interpretazione integrata di dati geofisici e geologici, in *73 Congress for Society and Geology Italy,* 29 sett-4 ott, Roma, p. 27.

Castro, R.R., Pacor, F., Puglia, R., Ameri, G., Letort, J., Massa, M. & Luzi, L., 2013. The 2012 May 20 and 29, Emilia earthquakes (Northern Italy) and the main aftershocks: S-wave attenuation, acceleration source functions and site effects, *Geophys. J. Int.,* **195**(1), 597–611.

CEN (European Committee for Standardization), 2004. Eurocode 8: design of structures for earthquake resistance, Part 1: General rules, seismic actions and rules for buildings (EN1998-1), Brussels, Belgium.

Cesca, S., Braun, T., Maccaferri, F., Passarelli, L., Rivalta, E. & Dahm, T., 2013. Source modelling of the M5-6 Emilia-Romagna, Italy, earthquakes (2012 May 20-29), *Geophys. J. Int.,* **193**(3), 1658–1672.

Chaljub, E., Komatitsch, D., Vilotte, J.P., Capdeville, Y., Valette, B. & Festa, G., 2007. Spectral element analysis in seismology, in *Advances in Wave Propagation in Heterogeneous Media,* vol. 48 of Advances in Geophysics, pp. 365–419, eds Wu, R.-S. & Maupin, V., Elsevier, Academic Press, London, UK.

Chaljub, E., Moczo, P., Tsuno, S., Bard, P.Y., Kristek, J., Käser, M., Stupazzini, M. & Kristekova, M., 2010. Quantitative comparison of four numerical predictions of 3D ground motion in the Grenoble valley, France, *Bull. seism. Soc. Am.,* **100**(4), 1427–1455.

Day, S. M. & Bradley, C. R., 2001. Memory-efficient simulation of anelastic wave propagation, *Bull. seism. Soc. Am.,* **91**(3), 520–531.

Day, S. M., Graves, R., Bielak, J., Dreger, D., Larsen, S., Olsen, K.B., Pitarka, A. & Ramirez-Guzman, L., 2008. Model for basin effects on long-period response spectra in Southern California, *Earthq. Spectra,* **24**(1), 257–277.

De Basabe, J.D., Sen, M.K. & Wheeler, M.F., 2008. The interior penalty discontinuous Galerkin method for elastic wave propagation: grid dispersion, *Geophys. J. Int.,* **175**(1), 83–93.

DPC-INGV Project S2, 2012. *Constraining Observations into Seismic Hazard,* funded by the Department of Civil Protection from 2012 to 2013, Italy. Available at: http://sites.google.com/site/ingvdpc2012progettos2/home.

Ewald, M., Igel, H., Hinzen, K.-G. & Scherbaum, F., 2006. Basin-related effects on ground motion for earthquake scenarios in the Lower Rhine Embayment, *Geophys. J. Int.,* **166**(1), 197–212.

Faccioli, E., Maggio, F., Paolucci, R. & Quarteroni, A., 1997. 2D and 3D elastic wave propagation by a pseudo-spectral domain decomposition method, *J. Seismol.,* **1**(3), 237–251.

Fantoni, R. & Franciosi, R., 2010. Tectono-sedimentary setting of the Po Plain and Adriatic foreland, *Rend. Fis. Acc. Lincei,* **21,** S197–S209.

Furumura, T. & Hayakawa, T., 2007. Anomalous propagation of long-period ground motions recorded in Tokyo during the 23 October 2004 M_W 6.6 Niigata-ken Chuetsu, Japan, earthquake, *Bull. seism. Soc. Am.,* **97**(3), 863–880.

Galli, P., Castenetto, S. & Peronace, E., 2012. *Rilievo Macrosismico MCS speditivo, Terremoti dell'Emilia—Maggio 2012, Tech. Rep., Dipartimento della Protezione Civile, Final Report.*

Gallovič, F., Kaser, M., Burjanek, J. & Papaioannou, C., 2010. Three-dimensional modeling of near-fault ground motions with nonplanar rupture models and topography: case of the 2004 Parkfield earthquake, *J. geophys. Res.,* **115**(B3), B03308, doi:10.1029/2008JB006171.

Göddeke, D., Komatitsch, D. & Möller, M., 2014. Finite and spectral element methods on unstructured grids for flow and wave propagation methods, in *Numerical Computations with GPUs,* chap. 9, pp. 183–206, ed. Kindratenko, V., Springer.

Govoni, A. *et al.*, 2014. The 2012 Emilia seismic sequence (Northern Italy): imaging the thrust fault system by accurate aftershock location, *Tectonophysics,* **622,** 44–55.

Graves, R.W., 2008. The Seismic response of the San Bernardino basin region during the 2001 Big Bear Lake earthquake, *Bull. seism. Soc. Am.,* **98**(1), 241–252.

Graves, R.W. & Wald, D.J., 2004. Observed and simulated ground motions in the San Bernardino basin region for the Hector Mine, California, earthquake, *Bull. seism. Soc. Am.,* **94**(1), 131–146.

Graves, R. *et al.*, 2011. CyberShake: a physics-based seismic hazard model for Southern California, *Pure appl. Geophys.,* **168**(3–4), 367–381.

Guidotti, R., Stupazzini, M., Smerzini, C., Paolucci, R. & Ramieri, P., 2011. Numerical study on the role of basin geometry and kinematic seismic source in 3D ground motion simulation of the 22 February 2011 M_W 6.2 Christchurch earthquake, *Seism. Res. Lett.,* **82**(6), 767–782.

Herrero, A. & Bernard, P., 1994. A kinematic self-similar rupture process for earthquakes, *Bull. seism. Soc. Am.,* **84**(4), 1216–1228.

Hesthaven, J. & Warburton, T., 2008. *Nodal Discontinuous Galerkin Methods,* vol. 54 of Texts in Applied Mathematics, Springer, Berlin.

Hisada, Y. & Bielak, J., 2003. A theoretical method for computing near-fault ground motions in layered half-spaces considering static offset due to surface faulting, with a physical interpretation of fling step and rupture directivity, *Bull. seism. Soc. Am.,* **93**(3), 1154–1168.

Käser, M. & Dumbser, M., 2006. An arbitrary high order discontinuous Galerkin method for elastic waves on unstructured meshes. I: The two-dimensional isotropic case with external source terms, *Geophys. J. Int.,* **166**(2), 855–877.

Koketsu, K., Miyake, H. & Afnimar Tanaka, Y., 2009. A proposal for a standard procedure of modeling 3D velocity structures and its application to the Tokyo Metropolitan area, Japan, *Tectonophysics,* **472,** 290–300.

Komatitsch, D. & Tromp, J., 1999. Introduction to the spectral-element method for 3-D seismic wave propagation, *Geophys. J. Int.,* **139**(3), 806–822.

Komatitsch, D., Liu, Q., Tromp, J., Suss, P., Stidham, C. & Shaw, J.H., 2004. Simulations of ground motion in the Los Angeles basin based upon the Spectral Element Method, *Bull. seism. Soc. Am.,* **94**(1), 187–206.

Komatitsch, D., Tsuboi, S. & Tromp, J., 2005. The spectral-element method in seismology, in *Seismic Earth: Array Analysis of Broadband Seismograms,* vol. 157 of Geophysical Monograph, pp. 205–228, eds Levander, A. & Nolet, G., American Geophysical Union, Washington DC, USA.

Lee, S.-J., Chen, H.-W., Liu, Q., Komatitsch, D., Huang, B.-S. & Tromp, J., 2008a. Three-dimensional simulations of seismic-wave propagation in the Taipei basin with realistic topography based upon the Spectral Element Method, *Bull. seism. Soc. Am.,* **98**(1), 253–264.

Lee, S.-J., Chen, H.-W. & Huang, B.-S., 2008b. Simulations of strong ground motion and 3D amplification effect in the Taipei basin by using a composite grid Finite Difference Method, *Bull. seism. Soc. Am.,* **98**(3), 1229–1242.

Luzi, L. *et al.*, 2013. Overview on the strong-motion data recorded during the May–June 2012 Emilia seismic sequence, *Seism. Res. Lett.,* **84**(4), 629–644.

Maday, Y., Mavriplis, C. & Patera, A.T., 1989. Nonconforming mortar element methods: application to spectral discretizations, in *Domain Decomposition Methods (Los Angeles, CA, 1988),* pp. 392–418, SIAM, Philadelphia, PA.

Maini, C., 2015. Near-source seismic displacement evaluation: from data processing to code provisions, *Master thesis,* Geotechnical Engineering, Politecnico di Milano.

Martelli, L. & Molinari, F., 2008. *Studio geologico finalizzato alla ricerca di potenziali serbatoi geotermici nel sottosuolo del comune di mirandola, Tech. Rep., Regione Emilia-Romagna, Servizio geologico sismico e dei suolo,* in Italian.

Mazzieri, I., Stupazzini, M., Guidotti, R. & Smerzini, C., 2013. SPEED: SPectral Elements in Elastodynamics with Discontinuous Galerkin: a non-conforming approach for 3D multi-scale problems, *Int. J. Numer. Method Eng.,* **95**(12), 991–1010.

Milana, G., Bordoni, P., Cara, F., Di Giulio, G., Hailemikael, S. & Rovelli, A., 2014. 1D velocity structure of the Po River plain (Northern Italy) assessed by combining strong motion and ambient noise data, *Bull. Earth. Eng.,* **12,** 2195–2209.

Moczo, P., Kristek, J. & Galis, M., 2014. *The Finite-Difference Modelling of Earthquake Motions: Waves and Ruptures,* Cambridge Univ. Press.

Molinari, I., Argnani, A., Morelli, A. & Basini, P., 2015. Development and testing of a 3D seismic velocity model of the Po Plain sedimentary basin, Italy, *Bull. seism. Soc. Am.,* **105**(2A), 753–764.

Molnar, S., Cassidy, J.F., Olsen, K.B., Dosso, S.E. & He, J., 2014. Earthquake ground motion and 3D Georgia basin amplification in Southwest British Columbia: shallow blind-thrust scenario earthquakes, *Bull. seism. Soc. Am.,* **104**(1), 301–320.

Munich, RE, 2015. *NatCatService,* http://www.munichre.com/natcatservice.

Olsen, K.B. *et al.*, 2006. Strong shaking in Los Angeles expected from southern San Andreas earthquake, *Geophys. Res. Lett.,* **33**(7), L07305, doi:10.1029/2005GL025472.

Olsen, K.B., Day, S.M., Minster, J.B., Cui, Y., Chourasia, A., Okaya, D., Maechling, P. & Jordan, T., 2008. TeraShake2: spontaneous rupture simulations of M_W 7.7 earthquakes on the Southern San Andreas Fault, *Bull. seism. Soc. Am.,* **98**(3), 1162–1185.

Olsen, K.B. *et al.*, 2009. ShakeOut-D: ground motion estimates using an ensemble of large earthquakes on the southern San Andreas fault with spontaneous rupture propagation, *Geophys. Res. Lett.,* **36**(4), L04303, doi:10.1029/2008GL036832.

Olsen, K.B. & Mayhew, J.E., 2010. Goodness-of-fit criteria for broadband synthetic seismograms, with application to the 2008 M_W 5.4 Chino Hills, California, earthquake, *Seimol. Res. Lett.,* **81**(5), 715–723.

Paolucci, R., Mazzieri, I., Smerzini, C. & Stupazzini, M., 2014. Physics-based earthquake ground shaking scenarios in large urban areas, in *Perspectives on European Earthquake Engineering and Seismology, Geotechnical, Geological and Earthquake Engineering,* vol. 34, chap. 10, pp. 331–359, ed. Ansal, A., Springer.

Patera, A.T., 1984. A spectral element method for fluid dynamics: laminar flow in a channel expansion, *J. Comput. Phys.,* **54**(3), 468–488.

Peyrusse, F., Glinsky, N., Gélis, C. & Lanteri, S., 2014. A nodal discontinuous galerkin method for site effects assessment in viscoelastic media-verification and validation in the nice basin, *Geophys. J. Int.,* **199**(1), 315–334.

Pezzo, G. *et al.*, 2013. Coseismic deformation and source modeling of the May 2012 Emilia (Northern Italy) earthquakes, *Seism. Res. Lett.,* **84**(4), 645–655.

Pieri, M. & Groppi, G., 1981. Subsurface geological structure of the Po Plain, Italy, *CNR, Prog. Final. Geod.,* **414,** 1–13.

Quarteroni, A., Sacco, R. & Saleri, F., 2007. *Numerical Mathematics,* vol. 37 of Texts in Applied Mathematics, 2nd edn., Springer-Verlag, Berlin.

RER, 1998. *Riserve Idriche Sotterranee della Regione Emilia-Romagna,* Servizio Geologico Sismico e dei Suoli & ENI-AGIP, Di Dio (ed.), S.EL.CA., Florence, 120 pp.

Rodgers, A., Petersson, N.A., Nilsson, S., Sjögreen, B. & McCandless, K., 2008. Broadband waveform modeling of moderate earthquakes in the San Francisco bay area and preliminary assessment of the USGS 3D seismic velocity model, *Bull. seism. Soc. Am.,* **98**(2), 969–988.

Roten, D., Olsen, K.B., Pechmann, J.C., Cruz-Atienza, V.M. & Magistrale, H., 2011. 3D simulations of M 7 earthquakes on the Wasatch Fault, Utah, Part I: Long-period (0–1 Hz) ground motion, *Bull. seism. Soc. Am.,* **101**(5), 2045–2063.

Roten, D., Olsen, K.B & Pechman, J.C., 2012. 3D simulations of M 7 earthquakes on the Wasatch Fault, Utah, Part II: Broadband (0–10 Hz) ground motions and nonlinear soil behavior, *Bull. seism. Soc. Am.,* **102**(5), 2008–2030.

Salvi, S. *et al.*, 2012. Activation of the SIGRIS monitoring system for ground deformation mapping during the Emilia 2012 seismic sequence, using COSMO-SkyMed InSAR data, *Ann. Geophys.,* **55**(4), doi:10.4401/ag-6181.

Scognamiglio, L. *et al.*, 2012. The 2012 Pianura Padana Emiliana seismic sequence: locations, moment tensors and magnitudes, *Ann. Geophys.,* **55**(4), 549–559.

Seriani, G., Priolo, E. & Pregarz, A., 1995. Modelling waves in anisotropic media by a spectral element method, *Proceedings of the Third International Conference on Mathematical and Numerical Aspects of Wave Propagation,* pp. 289–298, ed.Cohen, G., SIAM Philadephia, PA.

Smerzini, C. & Villani, M., 2012 Broadband numerical simulations in complex near field geological configurations: the case of the M_W 6.3 2009 L'Aquila earthquake, *Bull. seism. Soc. Am.,* **102**(6), 2436–2451.

Smerzini, C., Paolucci, R. & Stupazzini, M., 2011. Comparison of 3D, 2D and 1D approaches to predict long period earthquake ground motion in the Gubbio plain, Central Italy, *Bull. Earth. Eng.,* **9**(6), 2007–2029.

Stacey, R., 1988. Improved transparent boundary formulations for the elastic-wave equation, *Bull. seism. Soc. Am.,* **78**(6), 2089–2097.

Stupazzini, M., Paolucci, R. & Igel, H., 2009. Near-fault earthquake ground-motion simulation in the Grenoble valley by a high-performance spectral element code, *Bull. seism. Soc. Am.,* **99**(1), 286–301.

Taborda, R. & Bielak, J., 2014. Ground-motion simulation and validation of the 2008 Chino Hills, California, earthquake using different velocity models, *Bull. seism. Soc. Am.,* **104**(4), 1876–1898.

Tizzani, P. *et al.*, 2013. New insights into the 2012 Emilia (Italy) seismic sequence through advanced numerical modeling of ground deformation InSAR measurements, *Geophys. Res. Lett.,* **40**(10), 1971–1977.

Villani, M., Faccioli, E., Ordaz, M. & Stupazzini, M., 2014. High-resolution seismic hazard analysis in a complex geological configuration: the case of the Sulmona basin in Central Italy, *Earthq. Spectra,* **30**(4), 1801–1824.

Wang, H., Igel, H., Gallovič, F., Cochard, A. & Ewald, M., 2008. Source-related variations of ground motions in 3D media: application to the Newport-Inglewood fault, Los Angeles Basin, *Geophys. J. Int.,* **175**(1), 202–214.

Wilcox, L.C., Stadler, G., Burstedde, C. & Ghattas, O., 2010. A high-order discontinuous Galerkin method for wave propagation through coupled elastic-acoustic media, *J. Comput. Phys.,* **229**(24), 9373–9396.